HHS Public Access

Author manuscript

Bioorg Med Chem. Author manuscript; available in PMC 2023 September 01.

Published in final edited form as:

Bioorg Med Chem. 2022 September 01; 69: 116878. doi:10.1016/j.bmc.2022.116878.

2-Aminopyridines with a Shortened Amino Sidechain as Potent, Selective, and Highly Permeable Human Neuronal Nitric Oxide Synthase Inhibitors

Dhananjayan Vasu[†], **Huiying Li**[§], **Christine D. Hardy**[§], **Thomas L. Poulos**[*,§], **Richard B. Silverman**[*,†,¶]

[†]Department of Chemistry, Department of Molecular Biosciences, Chemistry of Life Processes Institute, Center for Developmental Therapeutics, Northwestern University, 2145 Sheridan Road, Evanston, Illinois 60208-3113, United States

[§]Departments of Molecular Biology and Biochemistry, Pharmaceutical Sciences, and Chemistry, University of California, Irvine, California 92697-3900, United States

[¶]Department of Pharmacology, Feinberg School of Medicine, Northwestern University, Chicago, Illinois 60611

Abstract

A series of potent, selective, and highly permeable human neuronal nitric oxide synthase inhibitors (hnNOS) based on the 2-aminopyridine scaffold with a shortened amino sidechain is reported. A rapid and simple protocol was developed to access these inhibitors in excellent yields. Neuronal nitric oxide synthase (nNOS) is a novel therapeutic target for the treatment of various neurological disorders. The major challenges in designing nNOS inhibitors in humans focus on potency, selectivity over other isoforms of nitric oxide synthases (NOSs), and blood-brain barrier permeability. In this context, we discovered a promising inhibitor, 6-(3-(4,4-difluoropiperidin-1-yl)propyl)-4-methylpyridin-2-amine dihydrochloride, that exhibits excellent potency for rat (K_i = 46 nM) and human nNOS (K_i = 48 nM), respectively, with 388-fold human eNOS and 135-fold human iNOS selectivity. It also displayed excellent permeability ($P_e = 17.3 \times 10^{-6}$ cm s^{-1}) through a parallel artificial membrane permeability assay, a model for blood-brain permeability. We found that increasing lipophilicity by incorporation of fluorine atoms on the backbone of the inhibitors significantly increased potential blood-brain barrier permeability. In addition to measuring potency, isoform selectivity, and permeability of NOS inhibitors, we also explored structure-activity relationships via structures of key inhibitors complexed to various isoforms of nitric oxide synthases.

[*]Corresponding authors: Thomas L. Poulos, poulos@uci.edu. Tel: +1 949 824 7020.; Richard B. Silverman, Agman@chem.northwestern.edu. Tel: +1 847 491 5653. Fax: +1 847 491 7713.

Declaration of Competing Interest

The authors declare no conflict of interest.

Appendix A. Supplementary material

Supplementary data to this article can be found online at https://doi.org/10.1016/j.bmc.2022XXXXX

1. Introduction

The gaseous free radical nitric oxide (NO) has emerged as an important cell signaling molecule involved in numerous physiological and pathological processes.[1–2] In human physiology, the role of NO is unique and regulates essential processes such as neurotransmission,[3] vasodilation,[4] smooth muscle relaxation,[5] and immune response.[6] In mammals, nitric oxide is produced endogenously through the oxidation of L-arginine to L-citrulline with the help of NADPH and molecular oxygen by three principal nitric oxide synthases (NOSs), namely, neuronal NOS (nNOS), endothelial NOS (eNOS), and inducible NOS (iNOS).[7] Neuronal NOS (nNOS) catalyzes the oxidation of L-arginine in the central nervous system (CNS) to produce NO, a critical neurotransmitter for neuronal communication.[8–10] Endothelial NOS (eNOS) is an isozyme of NOS that reduces blood pressure through relaxation of muscle.[11] Inducible NOS (iNOS), on the other hand, produces cytotoxic NO and is responsible for activating the immune system to destroy pathogens and microorganisms.[12]

In the last decade, the excessive production of nitric oxide by nNOS has been recognized as a key player in the induction and progression of neurodegenerative diseases. Although the normal activity of producing physiological levels[13] of NO by nNOS is important for neurotransmission, its overproduction is associated with the formation of the extremely reactive oxidant, peroxynitrite ($ONOO^-$),[14] in the presence of superoxide. nNOS has also been shown to be involved in several chronic neurodegenerative pathologies such as Alzheimer's disease (AD),[15] Parkinson's disease (PD),[16] Huntington's disease (HD),[17] amyotrophic lateral sclerosis (ALS),[18] neuronal damage during stroke,[19] as well as chronic headaches.[20] Finally, at high concentrations, NO can cause excessive nitration and/or nitrosylation of proteins, leading to their degradation and misfolding.[21]

The three mammalian NOSs show high homology (>50% amino acid identity) and are active only as homodimers.[7] Each monomer of NOS consists of a C-terminal reductase and an N-terminal oxygenase domain connected via a calmodulin-binding region. The C-terminal reductase domain contains the binding sites for reduced nicotinamide adenine dinucleotide phosphate (NADPH), flavin adenine dinucleotide (FAD), and flavin mononucleotide (FMN) and is responsible for transporting electrons to the iron center of the heme during biosynthesis of NO.[22] The N-terminal oxygenase domain contains the binding sites for noncatalytic zinc (Zn^{2+}), tetrahydrobiopterin (H_4B), and a heme-containing catalytic active site that binds the substrate, L-Arg.[7] In the active site, NOSs catalyze the oxidation of L-arginine to L-citrulline and release NO in the presence of NADPH and molecular oxygen. This crucial cascade reaction is initiated at the reductase domain by the two-electron donor, NADPH, to the electron acceptor, the iron center of heme in the oxygenase domain, through FAD and FMN with a series of proton transfers in the process.[23]

The inhibition of nNOS has shown promise in treating or preventing neuronal damage in animal models.[22] However, eNOS inhibition can cause cardiovascular problems and hypertension,[24] and iNOS inhibition can result in immune defense failure.[25] Therefore, inhibition of nNOS must be selective over the other isoforms to be a viable potential therapeutic approach for the treatment of neurodegenerative disorders.[7,26–27] Small

molecules that compete with the binding of L-Arg at the active site are one approach to inhibit nNOS. Design of such inhibitors can take advantage of slight but key differences in the active site structures of the three isoforms to build in nNOS selectivity.[28–29]

A major difficulty in treating central nervous system (CNS) diseases is ineffective drug delivery across the blood-brain barrier (BBB).[30–33] The BBB is located at the interface of the blood vessels and brain tissues and is formed by brain capillary endothelial cells creating a tight junction to protect the brain from circulating xenobiotic molecules. Small molecules account for the vast majority of CNS drugs primarily because of their ability to penetrate the phospholipid membrane of the blood-brain barrier by passive or carrier-mediated mechanisms.[34] In CNS drug development, factors such as: reduced molecular weight (MW < 500 Da; preferably nearer to 350–400 Da); increased lipophilicity (preferably ClogP <5); decreased topological polar surface area (TPSA < 76 $Å^2$; preferably 25–60 $Å^2$); the number of hydrogen bond donors, OH plus NH_2 count (HBD = 5; preferably 3); the number of hydrogen bond acceptors, O plus N atoms (HBA = 10; preferably 7); a reduced number of rotatable bonds (RB < 8; preferably nearer to 4–5); reduced pK_a of basic amino groups (pK_a 7.5–10.5; preferably near to 8.4); and reduced P-glycoprotein (P-gp) efflux (ER < 2), are expected to significantly improve blood-brain barrier permeability based on properties of successful CNS drugs.[32–33,35]

In particular, the number of rotatable bonds (NRB) is a direct indication of flexibility of a chemical molecule, and studies have shown that increased rotatable bond count has a negative effect on the permeation rate.[36] Reducing the number of rotatable bonds (NRB) not only improves the permeability rate but also oral bioavailability. Therefore, reducing molecular flexibility by lowering the number of rotatable bonds (NRB) is often an important consideration for improving BBB permeability.

Our laboratories have focused on the development of selective nNOS inhibitors for the treatment of neurodegenerative diseases for more than two decades, achieving big milestones in maintaining excellent potency while retaining high selectivity over other NOS isoforms and BBB permeability.[22,37–40] Our efforts in improving the pharmacokinetic (PK) properties of nNOS inhibitors using various medicinal chemistry approaches such as the incorporation of intramolecular hydrogen bonds (**1**),[41] suppressing amine basicity (**2**),[42] converting to prodrugs (**3**),[43] replacement of pharmacophores (**4–5**),[44–45] introduction of a double-pyridine pharmacophore (**6**),[46] incorporation of a pyridine linker (**7**),[47] and exchanging the pyridine linker with fluoroaryl (**8–9**),[37–38] have resulted in considerable improvements in the pharmacokinetic properties of NOS inhibitors (Figure 1).

We recently reported our first generation of nNOS inhibitors containing a 2-aminopyridine scaffold attached to a pyridine linker (**7**), which exhibits excellent potency with rat and human nNOS ($K_{i\ (rnNOS)}$ = 16 nM; $K_{i\ (hnNOS)}$ = 13 nM) as well as high selectivity over eNOS (hnNOS/heNOS = 1831). In addition, pharmacokinetic studies of **7** displayed very low cytochrome P450 inhibition, little human microsomal metabolism, and only 20% human plasma protein binding, all favorable properties. However, **7** displayed little or no Caco-2 permeability, predicting poor oral absorption and poor BBB permeability.[47] However, exchanging the pyridine linker for a fluorobenzene ring (**8**-**9**) yielded significant

improvement in membrane permeability while retaining high inhibitory activity. For example, **8** showed excellent potency and isoform selectivity toward human nNOS ($K_{i\ (hnNOS)}$ = 30 nM; hnNOS/heNOS = 2799), but it still displayed a high efflux ratio (ER = 5.9) by a bidirectional Caco-2 permeability assay.[37] Compound **9,** with one additional fluorine atom on the fluorobenzene middle linker and an azetidine ring in the tail compared to **8,** displayed excellent inhibition for human nNOS (K_i = 23 nM) and high selectivity over human eNOS (hn/he = 956) and human iNOS (hn/hi = 77) along with good brain penetration in PAMPA and Caco-2 permeability assays ($P_e = 16.3 \times 10^{-6}$ cm s^{-1}; $P_{app} = 17.0 \times 10^{-6}$ cm s^{-1}, respectively), and also had a lower efflux ratio (ER = 0.8).[38]

In continuation with these efforts, we report herein our development and optimization of a rapid and simple protocol for the synthesis of potent, selective, and highly permeable human neuronal nitric oxide synthase inhibitors based on the 2-aminopyridine scaffold, with the aim of improving cell-membrane permeability without sacrificing potency and isoform selectivity by lowering the number of rotatable bonds (NRB) in our molecules.

We performed several structural modifications to **9**, based on recent X-ray crystallographic analysis, to improve the potency, isoform selectivity, and permeability of the inhibitors (Figure 2). In our earlier reports, we demonstrated that the 2-aminopyridine scaffold was crucial for the key anchoring interactions of nNOS inhibitors with Glu-592 and Glu-597 at the active sites of rat nNOS and human nNOS, respectively.[37–38,40,47] Because of this, we retained the 2-aminopyridine head during further modification of our inhibitors. Structural modifications of this scaffold, especially at the tail amino functionality, was investigated to improve the bioavailability and selectivity of NOS inhibitors. Various strategies of structural modifications were employed to investigate their effect on biological activity. We found that the tail amino functionality is crucial for achieving high isoform selectivity after examining the inhibitory activity of **12**. Therefore, the major modifications in this study focused on exploring the diversity of the tail amino functionality, including increasing lipophilicity, reducing the rigidity of the linker, and modulating the pK_a of amine basicity.

First, reduction of the number of rotatable bonds within the molecule was investigated through truncation (**10–20**), by disconnecting the middle fluorobenzene linker and reattaching the remaining aliphatic tail amine portion directly to the 2-aminopyridine head. Second, length variation through homologation (**15–16**) from three carbons to four carbons between the 2- aminopyridine and tail amino functionality was examined. Third, methylation of the secondary amine to tertiary amine (**12**) was carried out in a strategy to improve permeability by reducing the number of H-bond donors. Fourth, increasing the rigidity of the molecule by introducing an alkyne moiety (**10, 13, 15, 17** and **19**) between the 2-aminopyridine and the tail amino functionality was carried out to improve permeability. Finally, modulation of the basicity of the amino tail functionality and maximizing the lipophilicity within the molecule (**17–20**) was used to improve selectivity and permeability. All synthesized compounds were investigated for their nNOS inhibitory activity and selectivity over eNOS and iNOS. In addition, all inhibitors were examined in a parallel artificial membrane permeability assay for blood-brain barrier permeability (PAMPA−BBB).

2. Results and Discussion

2.1. Chemistry

The general synthetic route to compounds **10–14**, and **17–20** is outlined in Scheme 1. Most of these compounds are accessed within two-three steps from the corresponding bromopyridines and alkyne precursors.

The alkyne precursors (**23**, **25**, and **27**) were prepared from propargyl bromide and the corresponding amine or amine hydrochloride through S_N2 substitution (Scheme 2).[58] The generated alkyne precursors (**23**, **25**, and **27**) were then coupled with 6-bromo-4-methylpyridin-2-amine (**21**, Scheme 1) via Sonogashira cross-coupling[48–49] to afford the desired alkynes (**10**, **13**, **17**, and **19**) in good to excellent yields. The flexible saturated version of NOS inhibitors is accessed by hydrogenation of the corresponding alkyne precursors (**10**, **13**, **17**, and **19**) using Pd/C[45] or $Pd(OH)_2/C$[50] with H_2.

The synthetic approaches to compounds **15–16** are outlined in Scheme 3. The Sonogashira cross-coupling reaction[51] between 6-bromo-4-methylpyridin-2-amine (**21**) and but-3-yn-1-ol was carried out at 120 °C under an inert atmosphere to obtain the corresponding alkynyl alcohol in 70% yield. The resulting primary alcohol is converted into the corresponding tosylate **28**, which is subsequently reacted with *N*,*N*-dimethylamine to afford the desired alkyne **15** in good yield. Hydrogenation of alkyne **15** was performed using Pd/C with H_2 to afford **16** in a 62% yield.

2.2. Biological activity

The inhibitory constant (K_i) of newly synthesized analogues (**10–20**) were measured using the NO-hemoglobin (Hb) capture assay.[52] All compounds were assayed against purified rat nNOS, human nNOS, human iNOS, and human eNOS for the evaluation of potency as well as isoform selectivity. Inhibitory activities of the compounds are summarized in Table 1. The ratio of hnNOS/rnNOS is made by the ratio of the K_i values of these inhibitors with human and rat nNOS. The ratio hn/rn is important for evaluating the potential translation of these inhibitors from preclinical to clinical studies. The isoform selectivity for nNOS over iNOS (hn/hi) and eNOS (hn/he) was obtained by comparing the K_i values of human nNOS with human iNOS and human eNOS, respectively.

As shown in Figure 2, the simplified versions of NOS inhibitors **(10–20)** were accessed through truncation by disconnecting the middle difluorobenzene linker and reattaching the remaining aliphatic tail amine portion directly to the 2-aminopyridine head. The structure−activity studies of newly synthesized compounds **(11–12)** (Table 1) revealed that the steric bulk on the amino tail plays a crucial role in achieving good isoform selectivity. For example, compound **12**, with a tertiary amine at the tail amino functionality, exhibits excellent potency for rat (K_i = 26 nM) and human nNOS (K_i = 29 nM), respectively, with 126-fold human eNOS and 98-fold human iNOS selectivity. In contrast, **11**, with a secondary amine, shows a higher potency than that of **12** with hnNOS; however, a drop in selectivity was observed with heNOS, suggesting that the tertiary amine is important for achieving good isoform selectivity in this series. Disappointingly, **12** displayed poor

membrane permeability (P_e = 2.0 × 10^{-6} cm s^{-1}) due to the lack of the lipophilic difluoroaryl linker as in parent lead **9**.

To improve the permeability of these inhibitors, we introduced C-F bonds at the backbone of the inhibitors. Interestingly, after installing a 4,4-difluoropiperidine at the tail amino functionality of **9**, as in **19**, we observed a dramatic increase in the permeability. In line with this result, we discovered the most promising inhibitor, i.e., compound **20,** which has a fluorinated tertiary amine at the tail and exhibits excellent potency for rat (K_i = 46 nM) and human nNOS (K_i = 48 nM), with 388-fold human eNOS and 135-fold human iNOS selectivity. Compound **20** also displayed excellent permeability (P_e = 17.3 × 10^{-6} cm s^{-1}) in the PAMPA-BBB assay (Table 2).

It is interesting to note that the nNOS inhibitors with rigid alkynes such as **10**, **13**, **17**, and **19** are less potent than their flexible saturated alkanes in potency and isoform selectivity. In contrast, the P_e values of those rigid alkynes (**10**, **13**, **17**, and **19**) are slightly better than their flexible alkane nNOS inhibitors in this series.

Next, the length variation by homologation (**15–16**) from three carbon to four carbons between the 2-aminopyridine and the tail amino functionality was examined. Compound **16** maintained good potency ($K_{i\ (hnNOS)}$ = 58 nM) and isoform selectivity (hn/hi = 132; hn/he = 127), although it suffered from poor permeability (P_e = 2.3 × 10^{-6} cm s^{-1}; Table 2). Compound **15** maintained good isoform selectivity (hn/hi = 91; hn/he = 216) but lost its potency by six-fold as compared to its flexible alkane version. Compound **15** shares similar permeability as its rigid alkyne analogues (**10**, **13**, **17**, and **19**) in the PAMPA-BBB assay.

2.3. Permeability

It is expected that reducing molecular flexibility through lowering the number of rotatable bonds (NRB) of an inhibitor should improve its membrane permeability (Table 2). To verify this hypothesis, lead **9** and its simplified versions **10–20** were examined in the PAMPA-BBB assay,[37–38,53] and the results were compared based on their effective permeability (P_e) values. The results indicate that the absence of a fluoroaryl segment in the simplified version of inhibitors **10–14** negatively impacted their membrane permeability. However, we found that installing fluorine atoms at the substituted amine tail considerably enhanced the permeability of NOS inhibitors (**17–20**). It is important to note that **19**, with an alkyne linker, showed the highest permeability (P_e = 21.1 × 10^{-6} cm s^{-1}) in this series due to the presence of fluorine atoms in the amine tail as well as maintenance of the alkyne rigidity in the molecule. Because of the increased flexibility of **20** its permeability (P_e = 17.3 × 10^{-6} cm s^{-1}) is considerably reduced relative to **19**. These results also indicate that maintaining rigidity in the molecule could further improve permeability. For example, permeability values were considerably increased for rigid alkynes **10**, **13**, **15, 17**, and **19**, compared to their more flexible versions **11**, **14**, **16**, **18,** and **20,** respectively. Based on the above experimental results, it is clear that maintaining rigidity and incorporating F atoms at the amine tail improve permeability without altering the potency and isoform selectivity of NOS inhibitors.

2.4. Structure-Activity Relationships

2.4.1 Truncation of lead 9—Reduction of the number of rotatable bonds within the molecule was investigated through truncation (**10–20**) by disconnecting the middle fluorobenzene linker and reattaching the remaining aliphatic tail amine portion directly to the 2-aminopyridine head. We showed in earlier reports[37–38,40,47] that the 2-aminopyridine ring was crucial for the key interactions of nNOS inhibitors with Glu-592 and Glu-597 at the active sites of rat nNOS and human nNOS, respectively. Similarly, the terminal tail amine also plays a crucial role in the interactions with heme propionates for achieving higher potency. The linker between the 2-aminopyridine head and the amine tail provides additional variations for SAR studies. In this truncated series of compounds, we tested different tail amines, from simple tertiary amines to saturated cyclic amines, and further introduced fluorines into the cyclic amine to adjust its basicity. Other changes include different linker lengths and a rigid alkyne versus a flexible alkane linker. The collected crystallographic data reveal the following key features of SAR information: (1) A shorter linker provides better binding affinity; (2) The rigid alkyne linker leads to poor binding due to steric clashes, even through compounds with a rigid linker exhibit better permeability; (3) Compound **20**, with a short flexible linker and a tail 4,4-difluoropiperidine ring, shows a unique binding mode resulting in both good potency and permeability.

First, we determined the crystal structures of rnNOS, hnNOS, and heNOS in complex with **12** that bears the *N,N*-dimethylaminopropyl side chain as the amine tail (Table 1 and Figure 3). The crystal structures of bound **12** revealed a unique inhibitor binding mode. In rnNOS (Figure 3A), in addition to the H-bonds from the 2-aminopyridine to Glu-592 and Trp-587, the tail tertiary amino group can approach the heme propionate A and form a H-bond directly. In contrast, the tail azetidine ring N atom in lead **9** forms a H-bond with the water sitting in between the H_4B and propionate A, as seen in Figure S1. This is the main difference between the fluorophenyl ring-containing inhibitors and the current simplified versions. The removal of the difluorophenyl ring in lead **9** also removes the H-bonding interaction of Tyr-562 and Tyr-567 in rnNOS and hnNOS, respectively. These interactions were essential to achieve high potency and selectivity in the previous series. However, removal of this portion of lead **9**, as depicted in the simplified NOS inhibitors, does not affect the potency significantly but had some unfavorable effects on isoform selectivity.

Compound **12** maintained excellent potency towards rnNOS (K_i = 26 nM) and hnNOS (K_i = 29 nM), even though it loses the additional binding interactions that originate from the difluorophenyl group in lead **9** ($K_{i\ (rnNOS)}$ = 26 nM and $K_{i\ (hnNOS)}$ = 23 nM). Similarly, **12** binds to hnNOS (Figure 3B) with its 2-aminopyridine head to form H-bonds with Glu-597 and Trp-592 and its tail amino group to propionate A. Compared with the rnNOS structure of **12**, the conformation of the tail amino linker in hnNOS is different: in rnNOS it is extended, while in hnNOS it is curled. The different conformation of the tail amino linker is due to the quite different orientation of the 2-aminopyridine ring in these structures. The reason for the difference is not clear; the side chain conformation of the anchoring Glu residue in these two structures is essentially the same.

Figure 3C shows the binding mode of **12** with human eNOS. Compound **12** binds well to human eNOS (K_i = 3362 nM). In addition to the H-bonds from the 2-aminopyridine to Glu-361 and Trp-356, the tail tertiary amino group also makes a H-bond directly with propionate A. Because of its better binding to heNOS, compound **12** displays an 8-fold drop in heNOS selectivity (hn/he = 126) as compared to lead **9** (hn/he = 956).[38] The orientation of the 2-aminopyridine ring of **12** in the structure with rnNOS is significantly different from that observed with heNOS, much more tilted from the heme plane in rnNOS than in heNOS. However, in all these cases (rnNOS, hnNOS, and heNOS), the tail tertiary amino group can still approach propionate A for a H-bond.

Next, we examined the effect of steric bulk on the amine tail to improve isoform selectivity. Compound **11** is the secondary amine variant of the tail functionality similarly positioned as the tertiary amino group of **12**. As shown in Figure 4, the binding interactions of **11** to hnNOS and heNOS are essentially the same. Compound **11** is capable of making a H-bond with propionate A in hnNOS, in addition to the other interactions such as the H-bonds to Glu-597 and Trp-592 with 2-aminopyridine. The advantage of the secondary amine in **11** is having fewer methyl groups compared to the tertiary amine in **12**, thus having fewer steric clashes with propionate A while making the H-bond. This result agrees with the finding of slightly better potency ($K_{i\ (hnNOS)}$ = 21 nM) of **11** relative to that of **12**. Similarly, in heNOS, **11** makes a H-bond with propionate A, along with two other H-bonds to Glu-361 and Trp-356 with the 2-aminopyridine. However, a drop in selectivity was observed with heNOS (hn/he = 70) as compared to **12** (hn/he = 126), because the secondary amine exhibits better binding to heNOS.

When the tail amino group is replaced by a piperazine ring, as in **14**, the binding affinity drops two-fold in rnNOS ($K_{i\ (rnNOS)}$ = 56 nM). The structure with this compound shows that one of the piperazine N atoms can approach for a H-bond to propionate D that has been bent over for the interaction (Figure 4 C). However, the flexibility of the piperazine ring of **14** is higher in the heNOS structure (Figure 4 D). A weaker H-bond is observed from the piperazine ring to propionate A, which is consistent with its much poorer affinity ($K_{i\ (heNOS)}$ = 12536 nM) compared to **11 (**$K_{i\ (heNOS)}$ = 1469 nM).

2.4.2. Homologation—Based on the information accumulated from **11** and **12**, we decided to incorporate a tertiary amine instead of a secondary amine as the tail amine functionality for future molecules in this truncated series. Further modification of **12** via homologation by increasing one-carbon (**16**) between the 2-aminopyridine and the tail amine functionality as represented in both the rigid alkyne (**15**) and its flexible saturated alkane (**16**) was investigated without further modification at the tertiary amine (*N*, *N*-dimethylamino group). The rigid alkyne (**15**) shows a slight improvement in heNOS selectivity (hn/he = 216) as well as permeability ($P_e = 4.7 \times 10^{-6}$ cm s^{-1}); however, its potency towards hnNOS was reduced by 11-fold relative to **12**. The available structure of hnNOS bound with **15** (Figure S2) indicates that the longer and rigid alkyne linker of **15** allows it to make a H-bond with propionate D rather than with propionate A as observed in **12**. This creates a steric clash at 3.0 Å from propionate A to the rigid linker, which drives up the binding energy leading to high K_i value (327 nM). Compound **16** showed about a 2-fold

drop in potency (K_i (hnNOS) = 58 nM), with a slight improvement in isoform selectivity (hn/hi = 132; hn/he = 127) compared to that of **12**, and it suffered from poor permeability (P_e = 2.3 × 10^{-6} cm s^{-1}; Table 2). The structure (Figure S2) shows that the flexible linker of **16** relaxes the clash between propionate A and the linker (3.1 – 3.2 Å); therefore, the affinity of **16** to hnNOS is significantly better than that of **15**.

2.4.3. Introducing rigidity—Based on the above results, we attempted to improve the permeability of these inhibitors by increasing the rigidity at the linker section of **12** by incorporating an alkyne moiety between the 2-aminopyridine and the tail amino functionality. We designed and synthesized the appropriate NOS inhibitors and investigated their permeability through a PAMPA-BBB assay.

As shown in Table 2, the rigid alkynes **10**, **13**, **15**, **17**, and **19** exhibited moderate to excellent permeability values with increasing rigidity. Unfortunately, there was also a negative effect on the binding affinity to hnNOS: the approximately 3-fold (**10**), 73-fold (**13**), 17-fold (**17**), and 49-fold **(19**) drop in potency with hnNOS reflects their lower binding affinity relative to that of **12.**

As shown in Figure 5 compound **10** retains its H-bonding interaction with propionate A in all three structures (rnNOS, hnNOS, and heNOS). While a 3-fold drop in affinity with rnNOS and hnNOS is not clearly explained, maintaining a rather high affinity to heNOS is agreeable with the good H-bond observed in the structure. When the tail secondary amine is replaced by a bulky piperazine ring as in **13** the binding affinity worsens significantly. To our surprise, in hnNOS one of the piperazine ring N atoms does form a H-bond with propionate D (Figure 6A). At a first glance, this seems to contradict the 73-fold affinity drop. By closely examining the enzyme-inhibitor interaction, the unfavorable clash (pink arrow) at about 3.0 Å observed between **13** and propionate A resulting from the rigidity of the alkyne linker could be responsible for the affinity loss. The poor affinity of **13** to heNOS does find support in the structure (Figure 6B). The tail piperazine ring is partially disordered and likely bends upward from propionates but close to Gln-247. In the heNOS structure, the clash (pink arrow) of 3.0 Å between **13** and propionate A is also present.

2.4.4. Increasing lipophilicity—Various lipophilic amine moieties at the tail functionality were chosen to enhance lipophilicity of **12** by introduction of C-F bonds in the backbone of the saturated cyclic amine functionality (**17–20**). Modulation of basicity of the amino tail functionality was examined to increase the lipophilicity of the molecules (**17–20**) for improved selectivity and permeability. Both rigid alkynes (**17** and **19**) and the corresponding flexible saturated alkanes (**18** and **20**) with 3,3-difluoroazetidine and 4,4-difluoropiperidine rings at the tail, were investigated. Interestingly, these analogues were shown to exhibit a large improvement in permeability of about 9 to 11-fold over parent compound **12**, based on their PAMPA-BBB permeability assay (Table 2). Rigid alkyne **19** was identified as the most permeable NOS inhibitor (P_e = 21.1 × 10^{-6} cm s^{-1}) in this series, likely because of the presence of C-F bonds in the tertiary amine tail as well as the maintenance of alkyne rigidity in the molecule.

However, the addition of fluorine atoms to parent **12** also causes considerable changes in the binding affinity to NOS. The binding interaction of **17** is shown in Figure 7. In both rnNOS and hnNOS the difluoroazetidine ring bends toward propionate D, pushing it away. In this way, the 3,3-difluoroazetidine N atom can instead make a H-bond with propionate A. Also, in this bent conformation, the rigid linker of **17** can avoid clashes with propionate A. These observations are consistent with its better affinity to rnNOS and hnNOS than **13** (Table 1). In the new position, forced by inhibitor binding, the propionate D can make a H-bond with His341, which stabilizes the loop of residues 339–347, which are often disordered in hnNOS structures. However, the azetidine ring in heNOS bends upward away from the propionates (Figure 7C), and the fluorine atom makes van der Waals contacts with Gln-338. The clashes (pink arrow) from the alkyne linker to propionate A remain.

Compound **19** bears a 4,4-difluoropiperidine ring at the tail of a rigid alkyne linker. In all three structures (rnNOS, hnNOS, and heNOS), the 4,4-difluoropiperidine ring bends upward away from the heme propionates (Figure 8). In all cases the clashes (pink arrow) between the rigid alkyne linker and propionate A are inevitable. The combination of the lack of H-bonding with the piperidine ring and the presence of the unfavorable clashes account for the drop in potency by about 61- and 49-fold observed with rnNOS and hnNOS, respectively, compared with **12** (Table 1). The reduction in the potency of **19** is very likely the result of both the decrease in the pK_a of the tail amino functionality as well as maintenance of alkyne rigidity, thereby diminishing electrostatic interactions with heme propionate A, which we also observed in an earlier study.[37] Being able to maintain the H-bond with propionate A gives **17** a 3-fold better affinity than **19** with both rnNOS and hnNOS (Table 1). However, better binding of **17** to heNOS than **19** has no clear explanation.

The X-ray crystal structures of **18** bound with all three NOSs (Figure 9) show a H-bond from the ring N atom of 3,3-difluoroazetidine to heme propionate A. Because of the more flexible linker in **18** than in **17,** establishing the H-bonding interactions with propionate A by twisting the linker does not generate the clashes that were seen for **17**. Keeping the lipophilicity but relaxing the rigidity of the linker proved crucial to finding the most promising NOS inhibitor in this series, compound **20**, that not only shows excellent membrane permeability (P_e = 17.3 × 10^{-6} cm s^{-1}) but also shows excellent potency for rat (K_i = 46 nM) and human nNOS (K_i = 48 nM), respectively, with 388-fold heNOS and 135-fold hiNOS selectivity (Table 1 and 2).

It is interesting to note that the binding interaction of **20** (Figure 10) is quite different from the other members of this series. The H-bond observed for **20** with propionate D in rat and human nNOS results because propionate D bends over to optimize the geometry for H-bonding with the ring N atom of the 4,4-difluoropiperidine ring. Propionate D in heNOS does not show this change of conformation when the tail amine of **20** approaches with its linker in a more extended conformation. Therefore, the H-bond between the 4,4-difluoropiperidine and propionate D is less optimized in heNOS. The potential nonbonded interaction between the bulky Phe-105 side chain and the fluorine atom of the 4,4-difluoropiperidine ring may play a role in this different behavior of H-bond formation in heNOS compared to that in hnNOS.

The structural observations for **20** are in good agreement with the observed higher potency and selectivity as compared to rigid analogue **19** because of its flexible nature (Table 1). A slight decrease in potency of **20** relative to that of **12** is very likely the result of its lower pK_a due to the presence of the 4,4-difluoropiperidine tail group. However, **20** exhibits a much better membrane permeability, having a P_e value of 17.3×10^{-6} cm s^{-1} relative to that of **12** ($P_e = 2.0 \times 10^{-6}$ cm s^{-1}). This suggests that achieving both higher potency and good permeability can be a delicate balance; i.e., a slight change in the skeleton of the inhibitor can alter its properties considerably. Overall, because of their flexible nature, **18** and **20** show better binding interactions than their rigid and linear linker analogues **17** and **19**, thereby increasing their potency and selectivity.

3. Conclusion

In summary, a series of potent, selective, and highly permeable human nNOS inhibitors based on the 2-aminopyridine scaffold with a shortened amino sidechain was designed and evaluated. A rapid and simple protocol was developed to access these inhibitors with excellent yields. Compound **20,** which has a reduced number of rotatable bonds, had outstanding properties that exhibit excellent potency for rat (K_i = 46 nM) and human nNOS (K_i = 48 nM), respectively, with 388-fold human eNOS and 135-fold human iNOS selectivity. Compound **20** also displayed excellent membrane permeability (P_e = 17.3×10^{-6} cm s^{-1}) through a parallel artificial membrane permeability assay modeling the blood-brain barrier (PAMPA-BBB). We found that addition of fluorine atoms at the backbone of the amine tail of the inhibitors greatly increased membrane permeability, suggesting that lipophilicity will be a key component of clinically useful nNOS inhibitors. Increasing rigidity in the molecule also had an overall positive impact on permeability; however, it also decreased potency and isoform selectivity. Finally, we show that X-ray crystal structures of representative inhibitors, including **20**, bound to NOS isoforms provide excellent interpretations for their properties in potency, isoform selectivity, and permeability.

4. Experimental section

Unless otherwise stated, all the described reactions were performed under an argon atmosphere. Anhydrous solvents such as THF, 1,4-dioxane, CH_2Cl_2, MeOH, Et_3N, and DMF were purchased directly from commercial sources. *N,N*-dimethylpropargylamine and *N*-methylpropargylamine were purchased from Sigma-Aldrich. Metal catalysts, especially tetrakis(triphenylphosphine)palladium(0) was purchased from Strem Chemicals. Other metal catalysts such as bis(triphenylphosphine)palladium(II) dichloride, copper(I) iodide, and Pd/C (10 wt. % loading (dry basis), matrix carbon powder, wet support) were purchased from Sigma-Aldrich. $Pd(OH)_2/C$ (20% on carbon, 60% water, wet support) was acquired from Acros Organics. Sonogashira cross-coupling reactions were performed using Chemglass pressure vessels. All reactions were monitored by thin-layer chromatography (TLC) using Merck TLC silica gel 60 F_{254}; 0.25 mm glass plates and components were visualized by ultraviolet light (254 nm) and/or $KMnO_4$ or phosphomolybdic acid stain. ^1H and ^{13}C NMR spectra were recorded on a Bruker Avance III NMR spectrometer with an operating frequency of 500 and 126 MHz, respectively, in $CDCl_3$, CD_3OD, or DMSO. Chemical shifts are reported in parts per million, and multiplicities are indicated by s =

singlet, d = doublet, t = triplet, q = quartet, sep = septet, dd = doublet of doublet, dt = doublet of triplet, m = multiplet, and br = broad resonance. Coupling constants "J" were reported in hertz. High-resolution mass spectral (HRMS) data were obtained on an Agilent 6210 LC-TOF spectrometer in the positive ion mode using electrospray ionization (ESI) with an Agilent G1312A high-performance liquid chromatography (HPLC) pump and an Agilent G1367B autoinjector at the Integrated Molecular Structure Education and Research Center (IMSERC), Northwestern University. Flash column chromatography was performed on an Agilent 971-FP automated flash purification system with a Varian column station and various SiliCycle cartridges (4−80 g, 40−63 μm, 60 Å). All compounds undergoing biological testing were >95% pure.

4.1. General procedure for the synthesis of NOS inhibitors

4.1.1. Synthesis of 6-(3-(4,4-difluoropiperidin-1-yl)propyl)-4-methylpyridin-2-amine dihydrochloride (20)—

Synthesis of 6-(3-(4,4-difluoropiperidin-1-yl)propyl)-4-methylpyridin-2-amine dihydrochloride (**20**) is representative (Scheme 1).

4.1.2. Synthesis of propargyl amines 23, 25, and 27—

Compounds **23, 25,** and **27** were prepared following a reported procedure with slight modifications (Scheme 2).[58] To a stirred suspension of 4,4-difluoropiperidine hydrochloride (0.500 mg, 3.170 mmol, 1.0 equiv) and K_2CO_3 (877 mg, 6.350 mmol, 2.0 equiv) in anhydrous CH_3CN (10 mL) at 25 °C, a solution of propargyl bromide (0.420 mL, 3.810 mmol, 80% in toluene, 1.2 equiv) in anhydrous CH_3CN (2 mL) was added. The mixture was allowed to stir at 25 °C for 8 h. After completion of the reaction as indicated by TLC, the reaction mixture was diluted with water and then extracted with DCM (3 × 15 mL). The combined organic layers were washed with 20 mL of brine, dried over Na_2SO_4, filtered, and concentrated in vacuo, provided propargyl amine **25** (260 mg, 1.650 mmol, 52%) as a yellow semisolid. The crude product was sufficiently pure to use in the next step without further purification. The same procedure was adopted for the synthesis of propargyl amines **23** (yellow oil, 243 mg, 1.850 mmol, 48%) and **27** (yellow solid, 367 mg, 2.660 mmol, 53%).

4.1.3. Typical procedure for Sonogashira cross-coupling reaction (compounds 10, 13, 17 and 19)—

The synthesis of 6-(3-(4,4-difluoropiperidin-1-yl)prop-1-yn-1-yl)-4-methylpyridin-2-amine (**19**) is representative (Scheme 1). A flame-dried pressure vessel containing 6-bromo-4-methylpyridin-2-amine (**21**) (260 mg, 1.380 mmol, 1.0 equiv), $Pd(PPh_3)_4$ (24 mg, 0.02 mmol, 1.5 mol%), and CuI (26 mg, 0.14 mmol, 10 mol%) was filled with argon using three vacuum-argon flush cycles to remove oxygen. To this, CH_3CN (4 mL, 0.25 M), Et_3N (0.770 mL, 5.520 mmol, 4.0 equiv), and 4,4-difluoro-1-(prop-2-yn-1-yl)piperidine (**25**) (260 mg, 1.650 mmol, 1.2 equiv) in CH_3CN (1.5 mL) were added, and the resulting mixture was stirred for 12 h at 120 °C. After completion of the reaction as indicated by TLC, the reaction mixture was cooled to 25 °C, filtered through Celite, and concentrated by rotary evaporation. Purification of the crude residue was performed by flash column chromatography eluting with hexane: EtOAc (20:80, v:v) for 10 min to remove any nonpolar residues and followed by the solvent mixture (DCM:CH_3OH:Et_3N, 80:10:10, v:v) for another 15 min to afford compound **19** (154 mg, 0.580 mmol, 42%) as a brown solid. **^{1}H NMR** (500 MHz, $CDCl_3$): δ 6.67 (s, 1 H), 6.27 (s, 1

H), 4.47 (bs, 2 H), 3.54 (s, 2 H), 2.71 (t, J = 5.0 Hz, 4 H), 2.19 (s, 3 H), 2.13 – 1.95 (m, 4 H). **^{13}C NMR** (126 MHz, $CDCl_3$): δ 158.4, 149.1, 140.5, 121.7 (t, J = 241.9 Hz), 119.4, 109.2, 85.4, 83.1, 49.3 (t, J = 5.7 Hz), 47.2 (t, J = 1.9 Hz), 34.1 (t, J = 22.7 Hz), 20.9. **HRMS** (ESI) Calcd for $C_{14}H_{18}F_2N_3$ [$(M+H)^+$]: 266.1463, found: 266.1470.

4.1.4. Typical procedure for hydrogenation (compounds 11–12, 14, 18, and 20)[50]—Compound **19** (154 mg, 0.580 mmol, 1.0 equiv) was diluted with CH_3OH (10 mL) and flushed with nitrogen before adding a catalytic amount of $Pd(OH)_2/C$ (62 mg; 40% of the weight of the substrate). The inert atmosphere of this heterogeneous mixture was replaced with a hydrogen balloon at room temperature and stirring was continued at 80 °C for 24 h. The crude mixture was then filtered through a pad of Celite, and the filtrate was concentrated under reduced pressure. The crude product was purified by flash column chromatography eluting with hexane: EtOAc (20:80 v:v) for 10 min to remove any nonpolar residues and followed by the solvent mixture (DCM:CH_3OH:Et_3N, 80:10:10, v:v) for 15 another min to afford **20** (42 mg, 0.16 mmol, 27%) as an off-white solid. **^{1}H NMR** (500 MHz, $CDCl_3$): δ 6.34 (s, 1 H), 6.15 (s, 1 H), 4.32 (s, NH_2, 2 H), 2.58 – 2.49 (m, 6 H), 2.45 – 2.38 (m, 2 H), 2.18 (s, 3 H), 2.01 – 1.92 (m, 4 H), 1.89 – 1.79 (m, 2 H). **^{13}C NMR** (126 MHz, $CDCl_3$): δ 160.0, 158.2, 149.2, 122.3 (t, J = 241.9 Hz), 114.4, 106.5, 57.3, 50.1 (t, J = 5.0 Hz), 35.8, 34.1 (t, J = 23.3 Hz), 27.3, 21.1. **HRMS** (ESI) Calcd for $C_{14}H_{22}F_2N_3$ [$(M+H)^+$]: 270.1776, found: 270.1786.

4.1.5. Synthesis of 4-methyl-6-(3-(methylamino)prop-1-yn-1-yl)pyridin-2-amine dihydrochloride (10)—Compound **10** was obtained in a similar manner to that described for the synthesis of compound **19** in Scheme 1. Yield: 286 mg (1.630 mmol, 61%); brown solid. **^{1}H NMR** (500 MHz, CD_3OD): δ 6.72 (s, 2 H), 3.28 – 3.20 (m, 2 H), 2.93 (s, 6 H), 2.84 (t, J = 7.8 Hz, 2 H), 2.38 (s, 3 H), 2.22 – 2.16 (m, 2 H). **^{13}C NMR** (126 MHz, CD_3OD): δ 159.1, 155.9, 148.5, 114.9, 111.3, 57.7 (2xC), 43.6, 30.3, 24.7, 22.0. **HRMS** (ESI) Calcd for $C_{10}H_{14}N_3$ [$(M+H)^+$]: 176.1182, found: 176.1177.

4.1.6. Synthesis of 4-methyl-6-(3-(methylamino)propyl)pyridin-2-amine dihydrochloride (11)—Compound **11** was obtained in a similar manner to that described for the synthesis of compound **20** in Scheme 1. The hydrogenation was performed using 10% Pd/C at 25 °C for 12 h. Yield: 202 mg (1.130 mmol, 89%); pale yellow solid. **^{1}H NMR** (500 MHz, CD_3OD): δ 6.69 (s, 1H), 6.68 (s, 1H), 3.13 – 3.04 (m, 2H), 2.92 (s, NH, 1H), 2.86 – 2.82 (m, 2H), 2.73 (s, 3H), 2.38 (s, 3H), 2.14 – 2.07 (m, 2H). **^{13}C NMR** (126 MHz, CD_3OD): δ 159.2, 156.0, 148.7, 114.8, 111.3, 49.2, 33.6, 30.4, 26.0, 22.0. **HRMS** (ESI) Calcd for $C_{10}H_{18}N_3$ [$(M+H)^+$]: 180.1495, found: 180.1469.

4.1.7. Synthesis of 6-(3-(dimethylamino)propyl)-4-methylpyridin-2-amine dihydrochloride (12)—Compound **12** was obtained in a similar manner to that described for the synthesis of compound **20** in Scheme 1. The hydrogenation was performed using 10% Pd/C at 60 °C for 24 h. Yield: 172 mg (0.890 mmol, 84%); brown solid. **^{1}H NMR** (500 MHz, CD_3OD): δ 6.72 (s, 2 H), 3.28 – 3.20 (m, 2 H), 2.93 (s, 6 H), 2.84 (t, J = 7.8 Hz, 2 H), 2.38 (s, 3 H), 2.22 – 2.16 (m, 2 H). **^{13}C NMR** (126 MHz, CD_3OD): δ 159.1, 155.9,

148.5, 114.9, 111.3, 57.7 (2xC), 43.6, 30.3, 24.7, 22.0. **HRMS** (ESI) Calcd for $C_{11}H_{20}N_3$ [$(M+H)^+$]: 194.1652, found: 194.1631.

4.1.8. Synthesis of 4-methyl-6-(3-(4-methylpiperazin-1-yl)prop-1-yn-1-yl)pyridin-2-amine dihydrochloride (13)—Compound **13** was obtained in a similar manner to that described for the synthesis of compound **19** in Scheme 1. Yield: 600 mg (2.460 mmol, 92%); yellow solid. **^{1}H NMR** (500 MHz, $CDCl_3$): δ 6.62 (s, 1 H), 6.22 (d, *J* = 1.5 Hz, 1 H), 3.50 (s, 2 H), 2.82 – 2.32 (m, 8 H), 2.27 (s, 3 H), 2.15 (s, 3 H). **^{13}C NMR** (126 MHz, $CDCl_3$): δ 158.4, 148.9, 140.6, 119.1, 108.8, 85.4, 83.1, 55.1, 52.0, 47.6, 46.1, 20.8. **HRMS** (ESI) Calcd for $C_{14}H_{21}N_4$ [$(M+H)^+$]: 245.1761, found: 245.1766.

4.1.9. Synthesis of 4-methyl-6-(3-(4-methylpiperazin-1-yl)propyl)pyridin-2-amine dihydrochloride (14)—Compound **14** was obtained in a similar manner to that described for the synthesis of compound **20** in Scheme 1. The hydrogenation was performed using 10% Pd/C at 25 °C for 24 h. Yield: 472 mg (1.900 mmol, 80%); pale yellow solid. **^{1}H NMR** (500 MHz, $CDCl_3$): δ 6.34 (s, 1 H), 6.14 (s, 1 H), 4.27 (s, 2 H), 2.73 – 2.33 (m, 11 H), 2.27 (s, 3 H), 2.18 (s, 4 H), 1.88 – 1.82 (m, 2 H). **^{13}C NMR** (126 MHz, $CDCl_3$): δ 160.3, 158.2, 149.1, 114.4, 106.4, 58.3, 55.3, 53.3, 46.2, 36.0, 27.1, 21.0. **HRMS** (ESI) Calcd for $C_{14}H_{25}N_4$ [$(M+H)^+$]: 249.2074, found: 249.2078.

4.1.10. Synthesis of 6-(3-(3,3-difluoroazetidin-1-yl)prop-1-yn-1-yl)-4-methylpyridin-2-amine dihydrochloride (17)—Compound **17** was obtained in a similar manner to that described for the synthesis of compound **19** in Scheme 1. Yield: 257 mg (1.080 mmol, 28%); brown solid. **^{1}H NMR** (500 MHz, $CDCl_3$): δ 6.69 (s, 1 H), 6.29 (s, 1 H), 4.46 (bs, 2 H), 3.77 (t, *J* = 12.5 Hz, 4 H), 3.62 (s, 2 H), 2.20 (s, 3 H). **^{13}C NMR** (126 MHz, $CDCl_3$): δ 158.5, 149.2, 140.2, 119.5, 116.4 (t, *J* = 274.7 Hz), 109.3, 85.9, 81.3, 62.5 (t, *J* = 23.3 Hz), 45.1, 20.9. **HRMS** (ESI) Calcd for $C_{12}H_{14}F_2N_3$ [$(M+H)^+$]: 238.1150, found: 238.1147.

4.1.11. Synthesis of 6-(3-(3,3-difluoroazetidin-1-yl)propyl)-4-methylpyridin-2-amine dihydrochloride (18)—Compound **18** was obtained in a similar manner to that described for the synthesis of compound **20** in Scheme 1. The hydrogenation was performed using 10% Pd/C at 25 °C for 8 h. Yield: 123 mg (0.510 mmol, 62%); brown solid. **^{1}H NMR** (500 MHz, $(CD_3)_2SO$, shows mixture of rotamers): δ (6.68 + 6.67 + 6.63 + 6.60 (s, 2 H)), 4.41 – 4.32 (m, 3 H), 3.71 (t, *J* = 12.5 Hz, 1 H), 3.10 – 2.99 (m, 2 H), 2.78 – 2.73 (m, 2 H), (2.28 +2.27 (s, 3 H)), 2.16 – 2.09 (m, 1 H), 1.93 – 1.87 (m, 1 H). **^{13}C NMR** (126 MHz, $(CD_3)_2SO$, shows mixture of rotamers): 156.1 (s, 1xC merged), 154.2 (s, 1xC merged, (147.7 + 147.5, s, 1xC), (118.4 (t, *J* = 243.8 Hz) + 114.8 (t, *J* = 269.4 Hz), 1xCF_2), (112.8 +112.7 (s, 1xCH)), (109.4 + 109.3 (s, 1xCH)), (63.5 (t, *J* = 26.9 Hz, 1xCH_2 merged), 54.3 (s, 1xCH_2), 47.5 (t, *J* = 25.8 Hz, 1xCH_2), 46.8 (s, 1xCH_2), 43.2 (t, *J* = 27.1 Hz, 1xCH_2), (29.0 + 28.9 (s, 1xCH_2)), (24.1 + 23.7 (s, 1xCH_2)), (21.6 + 21.5 (s, 1xCH_3)). **HRMS** (ESI) Calcd for $C_{12}H_{18}F_2N_3$ [$(M+H)^+$]: 242.1463, found: 242.1462.

4.2. Synthesis of 4-(6-amino-4-methylpyridin-2-yl)but-3-yn-1-yl 4-methylbenzenesulfonate (28)

Compound **28** was prepared following a reported procedure with slight modifications (Scheme 3).[51] A flame-dried pressure vessel containing 6-bromo-4-methylpyridin-2-amine (**21**) (1.000 g, 5.350 mmol), $Pd(PPh_3)_4$ (123 mg, 0.107 mmol) and CuI (102 mg, 0.535 mmol) was filled with argon using three vacuum-argon flush cycles to remove oxygen. To this, CH_3CN (18 mL, 0.25 M), Et_3N (2.98 mL, 21.400 mmol), and But-3-yn-1-ol (0.506 mL, 10.700 mmol) in CH_3CN (3.4 mL) were added and the resulting mixture was stirred for18 h at 120 °C. After completion of the reaction as indicated by TLC, the reaction mixture was cooled to 25 °C, filtered through Celite, and concentrated in a rotary evaporator. Purification of the crude residue was performed by flash column chromatography eluting with hexane: EtOAc (20:80, v:v) for 10 min to remove any nonpolar residues and followed by the solvent mixture (DCM:CH_3OH:Et_3N, 80:10:10, v:v) for another 15 min to afford 4-(6-amino-4-methylpyridin-2-yl)but-3-yn-1-ol (660 mg, 3.750 mmol, 70%) as a brown solid. **^{1}H NMR** (500 MHz, $CDCl_3$): 6.62 (s, 1 H), 6.28 (s, 1 H), 3.80 (t, *J* = 6.3 Hz, 2 H), 2.66 (t, *J* = 6.3 Hz, 2H), 2.18 (s, 3 H). **^{13}C NMR** (126 MHz, $CDCl_3$): 158.3, 149.3, 140.7, 119.0, 109.0, 86.3, 82.0, 60.9, 23.9, 20.9. **LRMS** (ESI) Calcd for $C_{10}H_{13}N_2O$ [$(M+H)^+$]: 177.10, found: 178.54. To a stirred solution of 4-(6-amino-4-methylpyridin-2-yl)but-3-yn-1-ol (650 mg, 3.690 mmol) in dry DCM (20 mL) at 0 °C was added TsCl (740 mg, 3.870 mmol), 4-(Dimethylamino)pyridine (45 mg, 0.37 mmol) and Et_3N (0.620 mL, 4.420 mmol). After the addition, the reaction mixture was slowly warmed to room temperature and stirred for 8 h. After completion of the reaction as indicated by TLC, the reaction mixture was diluted with 1% aqueous K_2CO_3 (50 mL) and extracted with DCM (2 × 20 mL). The combined organic layer was then dried over Na_2SO_4 and concentrated in vacuo. The crude product was purified by flash column chromatography eluting with hexane: EtOAc (20:80, v:v) to EtOAc (100) to afford **28** (650 mg, 1.970 mmol, 53%) as yellow solid. **^{1}H NMR** (500 MHz, $CDCl_3$): δ 7.80 (d, *J* = 8.3 Hz, 2 H), 7.35 – 7.28 (m, 2 H), 6.63 – 6.54 (m, 1 H), 6.27 (t, *J* = 1.1 Hz, 1 H), 4.39 (s, 2 H), 4.16 (t, *J* = 7.3 Hz, 2 H), 2.77 (t, *J* = 7.3 Hz, 2 H), 2.43 (s, 3 H), 2.19 (s, 3 H). **^{13}C NMR** (126 MHz, $CDCl_3$): 158.3, 149.1, 145.1, 140.5, 132.8, 130.1, 128.2, 119.2, 109.1, 82.6 (2xC), 67.5, 21.8, 21.0, 20.4. **LRMS** (ESI) Calcd for $C_{17}H_{19}N_2O_3$ [$(M+H)^+$]: 331.11, found: 331.25.

4.2.1. Synthesis of 6-(4-(dimethylamino)but-1-yn-1-yl)-4-methylpyridin-2-amine dihydrochloride (15)—

Compound **15** was prepared following a reported procedure with slight modifications (Scheme 3).[51] To a stirred solution of **28** (500 mg, 1.510 mmol) and K_2CO_3 (1.050 g, 7.570 mmol) in anhydrous CH_3CN (10 mL) was added dimethylamine (0.910 mL, 1.820 mmol, 2 M in THF) at 25 °C. The resulting heterogeneous mixture was then heated to 80 °C for 9 h. After completion of reaction as indicated by TLC, the reaction mixture was cooled to room temperature, diluted with water, and the organic layer was extracted with ether (2 × 20 mL), followed by DCM:*i*PrOH (9:1 v:v; 1 × 20 mL). The combined organic layer was then dried over Na_2SO_4 and concentrated in vacuo. Purification of the crude residue was performed by flash column chromatography eluting with hexane: EtOAc (10:90, v:v) for 10 min to remove any nonpolar residues and followed by the solvent mixture (DCM:CH_3OH:Et_3N, 80:10:10, v:v) for another 15 min to afford **15** (210 mg, 1.030 mmol, 68%) as a brown oil. **^{1}H NMR** (500 MHz, $CDCl_3$): δ 6.61 (s, 1 H),

6.23 (d, 1 H), 4.42 (bs, NH_2, 2 H), 2.67 – 2.50 (m, 4 H), 2.26 (s, 6 H), 2.17 (s, 3 H). **^{13}C NMR** (126 MHz, $CDCl_3$): δ 158.3, 149.0, 141.2, 118.9, 108.6, 87.3, 81.2, 58.1, 45.3, 20.9, 18.3. **HRMS** (ESI) Calcd for $C_{12}H_{18}N_3$ [$(M+H)^+$]: 204.1495, found: 204.1498.

4.2.2. Synthesis of 6-(4-(dimethylamino)butyl)-4-methylpyridin-2-amine dihydrochloride (16)—Compound **16** was prepared following a reported procedure with slight modifications (Scheme 3).[45] Compound **15** (130 mg, 0.640 mmol) was diluted with dry CH_3OH (15 mL; degassed) and flushed with nitrogen before adding a catalytic amount of Pd/C (13 mg; 10% of the weight of the substrate). The inert atmosphere of this heterogeneous mixture was replaced with a hydrogen balloon at room temperature and continued the stirring at the same temperature for 24 h. The crude mixture was then filtered through a pad of Celite, and the filtrate was concentrated under reduced pressure. The crude product was purified by reverse phase flash column chromatography eluting with CH_3CN:H_2O (10:90, v:v) to CH_3CN:H_2O (30:70, v:v) to afford **16** (82 mg, 0.40 mmol, 62%) as a yellow oil. **^{1}H NMR** (500 MHz, $CDCl_3$): δ 6.35 (s, 1 H), 6.14 (s, 1 H), 4.30 (bs, NH_2, 2 H), 2.63 – 2.50 (m, 2 H), 2.33 – 2.23 (m, 2 H), 2.20 (s, 6 H), 2.18 (s, 3 H), 1.72 – 1.58 (m, 2 H), 1.58 – 1.43 (m, 2 H). **^{13}C NMR** (126 MHz, $CDCl_3$): δ 160.5, 158.2, 149.2, 114.4, 106.4, 59.8, 45.7, 38.1, 27.8, 27.7, 21.1. **HRMS** (ESI) Calcd for $C_{12}H_{22}N_3$ [$(M+H)^+$]: 208.1808, found: 208.1808.

Supplementary Material

Refer to Web version on PubMed Central for supplementary material.

Acknowledgments

We are grateful for the generous support from the National Institutes of Health (R35GM131788 to R.B.S., GM057353 and GM131920 to T.L.P.). We thank Radoslaw T. Chrzanowski for assistance in the MOE docking studies. This work made use of the IMSERC at Northwestern University, which has received support from the Soft and Hybrid Nanotechnology Experimental (SHyNE) Resource (NSF ECCS-2025633); the State of Illinois and International Institute for Nanotechnology (IIN). We also thank the beamline staff at SSRL and ALS for their assistance during the remote X-ray diffraction data collections.

References:

(1). Kerwin JF Jr.; Lancaster JR; Feldman PL Nitric oxide: a new paradigm for second messengers. J. Med. Chem 1995, 38, 4343–4362. [PubMed: 7473563]

(2). Vallance P, Leiper J Blocking NO synthesis: how, where and why? Nat. Rev. Drug Discovery 2002, 1, 939–950. [PubMed: 12461516]

(3). Vincent SR Nitric oxide: a radical neurotransmitter in the central nervous system. Prog. Neurobiol 1994, 42, 129–160. [PubMed: 7480785]

(4). Palmer RM; Ferrige AG; Moncada S Nitric oxide release accounts for the biological activity of endothelium-derived relaxing factor. Nature 1987, 327, 524–526. [PubMed: 3495737]

(5). Ignarro LJ; Lippton H; Edwards JC; Baricos WH; Hyman AL; Kadowitz PJ; Gruetter CA Mechanism of vascular smooth muscle relaxation by organic nitrates, nitrites, nitroprusside and nitric oxide: evidence for the involvement of S-nitrosothiols as active intermediates. J. Pharmacol. Exp. Ther 1981, 218, 739–749. [PubMed: 6115052]

(6). Bogdan C Nitric oxide and the immune response. Nat. Immunol 2001, 2, 907–916. [PubMed: 11577346]

(7). Alderton WK, Cooper CE, Knowles RG Nitric oxide synthases: structure, function and inhibition. Biochem. J 2001, 357, 593–615. [PubMed: 11463332]

(8). Barañano DE; Snyder SH Neural roles for heme oxygenase: contrasts to nitric oxide synthase. Proc. Natl. Acad. Sci. U.S.A 2001, 98, 10996–11002. [PubMed: 11572959]

(9). Esplugues JV NO as a signalling molecule in the nervous system. Br J Pharmacol 2002, 135, 1079–1095. [PubMed: 11877313]

(10). Wang Y; Newton DC; Marsden PA Neuronal NOS: Gene Structure, mRNA Diversity, and Functional Relevance. Crit. Rev. Neurobiol 1999, 13, 21–43. [PubMed: 10223522]

(11). Roe ND; Ren J Nitric oxide synthase uncoupling: a therapeutic target in cardiovascular diseases. Vasc. Pharmacol 2012, 57, 168–172.

(12). Karpuzoglu E; Ahmed SA Estrogen regulation of nitric oxide and inducible nitric oxide synthase (iNOS) in immune cells: implications for immunity, autoimmune diseases, and apoptosis. Nitric Oxide 2006, 15, 177–186. [PubMed: 16647869]

(13). Hall CN; Garthwaite J What is the real physiological NO concentration in vivo? Nitric Oxide 2009, 21, 92–103. [PubMed: 19602444]

(14). Torreilles F; Salman-Tabcheh S; Guérin M; Torreilles J Neurodegenerative disorders: the role of peroxynitrite. Brain Res. Rev 1999, 30, 153–163. [PubMed: 10525172]

(15). Dorheim M-A; Tracey WR; Pollock JS; Grammas P Nitric oxide synthase activity is elevated in brain microvessels in Alzheimer′ s disease. Biochem. Biophys. Res. Commun 1994, 205, 659–665. [PubMed: 7528015]

(16). Zhang L; Dawson VL; Dawson TM Role of nitric oxide in Parkinson's disease. Pharmacol. Ther 2006, 109, 33–41. [PubMed: 16005074]

(17). Norris PJ; Waldvogel HJ; Faull RLM; Love DR; Emson PC Decreased neuronal nitric oxide synthase messenger RNA and somatostatin messenger RNA in the striatum of Huntington's disease. Neuronsicence 1996, 72, 1037–1047.

(18). Drechsel DA; Estévez AG; Barbeito L; Beckman JS Nitric oxide-mediated oxidative damage and the progressive demise of motor neurons in ALS. Neurotoxic. Res 2012, 22, 251–264.

(19). Sims NR; Anderson MF Mitochondrial contributions to tissue damage in stroke. Neurochem. Int 2002, 40, 511–526. [PubMed: 11850108]

(20). Ashina M Nitric oxide synthase inhibitors for the treatment of chronic tension-type headache Exp. Opin. Pharmacother 2002, 3, 395–399.

(21). Uehara T; Nakamura T; Yao D; Shi Z-Q; Gu Z; Ma Y; Masliah E; Nomura Y; Lipton SA *S*-Nitrosylated protein-disulphide isomerase links protein misfolding to neurodegeneration. Nature 2006, 441, 513–517. [PubMed: 16724068]

(22). Mukherjee P; Cinelli MA; Kang S; Silverman RB Development of nitric oxide synthase inhibitors for neurodegeneration and neuropathic pain. Chem. Soc. Rev 2014, 43, 6814–6838. [PubMed: 24549364]

(23). Feng C Mechanism of Nitric Oxide Synthase regulation: electron transfer and interdomain interactions. Coord. Chem. Rev 2012, 256, 393–411. [PubMed: 22523434]

(24). Kobayashi Y; Ikeda K; Shinozuka K; Nara Y; Yamori Y; Hattori K L-nitroarginine increases blood pressure in the rat. Clin. Exp. Pharmacol. Physiol 1991, 18, 397–399. [PubMed: 1914242]

(25). Cinelli MA; Do HT; Miley GP; Silverman RB Inducible nitric oxide synthase: Regulation, structure, and inhibition, Med. Res. Rev 2020, 40, 158–189. [PubMed: 31192483]

(26). Southan GJ; Szabo C Selective pharmacological inhibition of distinct nitric oxide synthase isoforms. Biochem. Pharmacol 1996, 51, 383–394. [PubMed: 8619882]

(27). Babu BR; Griffith OW Design of isoform-selective inhibitors of nitric oxide synthase. Curr. Opin. Chem. Biol 1998, 2, 491–500. [PubMed: 9736922]

(28). Silverman RB Design of selective neuronal nitric oxide synthase inhibitors for the prevention and treatment of neurodegenerative diseases. Acc. Chem. Res 2009, 42, 439–451. [PubMed: 19154146]

(29). Poulos TL; Li H Structural basis for isoform-selective inhibition in nitric oxide synthase. Acc. Chem. Res 2013, 46, 390–398. [PubMed: 23030042]

(30). Di L; Rong H; Feng B Demystifying brain penetration in central nervous system drug discovery. J. Med. Chem 2013, 56, 2–12. [PubMed: 23075026]

(31). Misra A; Ganesh S; Shahiwala A; Shah SP Drug delivery to the central nervous system: a review, J Pharm Pharm Sci 2003, 6, 252–73. [PubMed: 12935438]

(32). Rankovic Z CNS drug design: balancing physicochemical properties for optimal brain exposure. J. Med. Chem 2015, 58, 2584–2608. [PubMed: 25494650]

(33). Wager TT; Hou X; Verhoest PR; Villalobos A Moving beyond rules: the development of a central nervous system multiparameter optimization (CNS MPO) approach to enable alignment of druglike properties. ACS Chem. Neurosci 2010, 1, 435–449. [PubMed: 22778837]

(34). Mikitsh JL; Chacko A-M Pathways for Small Molecule Delivery to the Central Nervous System across the Blood-Brain Barrier. Perspect Medicin Chem, 2014, 6, 11–24. [PubMed: 24963272]

(35). Wager TT; Chandrasekaran RY; Hou X; Troutman MD; Verhoest PR; Villalobos A; Will Y Defining Desirable Central Nervous System Drug Space through the Alignment of Molecular Properties, in Vitro ADME, and Safety Attributes. ACS Chem. Neurosci, 2010, 1, 420–434. [PubMed: 22778836]

(36). Veber DF; Johnson SR; Cheng H-Y; Smith BR; Ward KW; Kopple KD Molecular properties that influence the oral bioavailability of drug candidates, J. Med. Chem 2002, 45, 2615–2623. [PubMed: 12036371]

(37). Do HT; Wang H-Y; Li H; Chreifi G; Poulos TL; Silverman RB Improvement of Cell Permeability of Human Neuronal Nitric Oxide Synthase Inhibitors Using Potent and Selective 2-Aminopyridine-Based Scaffolds with a Fluorobenzene Linker. J. Med. Chem 2017, 60, 9360–9375. [PubMed: 29091437]

(38) <j/>. Do HT; Li H; Chreifi G; Poulos TL; Silverman RB Optimization of Blood−Brain Barrier Permeability with Potent and Selective Human Neuronal Nitric Oxide Synthase Inhibitors Having a 2−Aminopyridine Scaffold. J. Med. Chem 2019, 62, 2690–2707. [PubMed: 30802056]

(39). Ji H; Stanton BZ; Igarashi J; Li H; Martásek P; Roman LJ; Poulos TL; Silverman RB Minimal pharmacophoric elements and fragment hopping, an approach directed at molecular diversity and isozyme selectivity. Design of selective neuronal nitric oxide synthase inhibitors. J. Am. Chem. Soc 2008, 130, 3900–3914. [PubMed: 18321097]

(40). Kang S; Li H; Tang W; Martásek P; Roman LJ; Poulos TL; Silverman RB 2-Aminopyridines with a truncated side chain to improve human neuronal nitric oxide synthase inhibitory potency and selectivity. J. Med. Chem 2015, 58, 5548–5560. [PubMed: 26120733]

(41). Labby KJ; Xue F; Kraus JM; Ji H; Mataka J; Li H; Martásek P; Roman LJ; Poulos TL; Silverman RB Intramolecular hydrogen bonding: a potential strategy for more bioavailable inhibitors of neuronal nitric oxide synthase. Bioorg. Med. Chem 2012, 20, 2435–2443. [PubMed: 22370337]

(42). Xue F; Li H; Delker SL; Fang J; Martásek P; Roman LJ; Poulos TL; Silverman RB Potent, highly selective, and orally bioavailable gem-difluorinated monocationic inhibitors of neuronal nitric oxide synthase. J. Am. Chem. Soc 2010, 132, 14229–14238. [PubMed: 20843082]

(43). Silverman RB; Lawton GR; Ranaivo HR; Chico LK; Seo J; Watterson DM Effect of potential amine prodrugs of selective neuronal nitric oxide synthase inhibitors on blood−brain barrier penetration. Bioorg. Med. Chem 2009, 17, 7593–7605. [PubMed: 19796958]

(44). Mukherjee P; Li H; Sevrioukova I; Chreifi G; Martásek P; Roman LJ; Poulos TL; Silverman RB Novel 2,4-disubstituted pyrimidines as potent, selective, and cell-permeable inhibitors of neuronal nitric oxide synthase. J. Med. Chem 2015, 58, 1067–1088. [PubMed: 25489882]

(45). Cinelli MA; Li H; Chreifi G; Poulos TL; Silverman RB Nitrile in the hole: discovery of a small auxiliary pocket in neuronal nitric oxide synthase leading to the development of potent and selective 2-aminoquinoline inhibitors. J. Med. Chem 2017, 60, 3958–3978. [PubMed: 28422508]

(46). Nitric Oxide Synthase Inhibitors That Interact with Both Heme Propionate and Tetrahydrobiopterin Show High Isoform Selectivity. Kang S; Tang W; Li H; Chreifi G; Martásek P; Roman LJ; Poulos TL; Silverman RB J. Med. Chem 2014, 57, 4382–4396. [PubMed: 24758147]

(47). Wang H-Y; Qin Y; Li H; Roman LJ; Martásek P; Poulos TL; Silverman RB Potent and selective human neuronal nitric oxide synthase inhibition by optimization of the 2-aminopyridine based scaffold with a pyridine linker. J. Med. Chem 2016, 59, 4913–4925. [PubMed: 27050842]

(48). Sonogashira K; Tohda Y; Hagihara N A convenient synthesis of acetylenes: Catalytic substitutions of acetylenic hydrogen with bromoalkenes, iodoarenes and bromopyridines. Tetrahedron Lett 1975, 16, 4467–4470.

(49). Feuerstein M; Doucet H; Santelli M Sonogashira reaction of heteroaryl halides with alkynes catalysed by a palladium-tetraphosphine complex. J. Mol. Catal. Chem 2006, 256, 75–84.

(50). Angle SR; Henry RM Synthesis of enantiopure Indolizidine alkaloids from *a*-amino acids: Total synthesis of (−)-Indolizidine 167B, J. Org. Chem 1997, 62, 8549–8552. [PubMed: 11672001]

(51). Wagner M; Schepmann D; Ametamey SM; Wünsch B Modification of the 4-phenylbutyl side chain of potent 3-benzazepine-based GluN2B receptor antagonists, Bioorg. Med. Chem 2019, 27, 3559–3567. [PubMed: 31255496]

(52). Hevel JM; Marletta MA [25] Nitric-oxide synthase assays. Methods Enzymol 1994, 233, 250–258. [PubMed: 7516999]

(53). Di L; Kerns EH; Fan K; McConnell OJ; Carter GT High throughput artificial membrane permeability assay for blood− brain barrier. Eur. J. Med. Chem 2003, 38, 223–232. [PubMed: 12667689]

(54). Gürdere MB; Budak Y; Ceylan M Synthesis of 2,3,4,5-tetraphenylfuran, -thiophene and -pyrrole from toluene, Asian J. Chem 2008, 20, 1425–1430.

(55). Das S; Ko N; Lee E; Kim SE; Lee BC. Stereoselective three-component cascade synthesis of α-substituted 2,4-dienamides from *gem*-difluorochloro ethanes, Chem. Commun, 2019, 55, 14355–14358.

(56). McPherson CG, Caldwell N, Jamieson C, Simpson I, Watson AJB Amidation of unactivated ester derivatives mediated by trifluoroethanol, Org. Biomol. Chem, 2017, 15, 3507–3518. [PubMed: 28393949]

(57). Terry CA; Fernández M-J, Gude L; Lorente A; Grant KB Physiologically relevant concentrations of NaCl and KCl increase DNA photocleavage by an N-substituted 9-aminomethylanthracene dye, Biochemistry, 2011, 50, 10375–10389. [PubMed: 22014335]

(58). Di Porzio A; Galli U; Amato J; Zizza P; Iachettini S; Iaccarino N; Marzano S; Santoro F; Brancaccio D; Carotenuto A; De Tito S; Biroccio A; Pagano B; Tron GC; Randazzo A Synthesis and Characterization of Bis-Triazolyl-Pyridine Derivatives as Noncanonical DNA-Interacting Compounds. Int. J. Mol. Sci 2021, 22, 11959. [PubMed: 34769387]

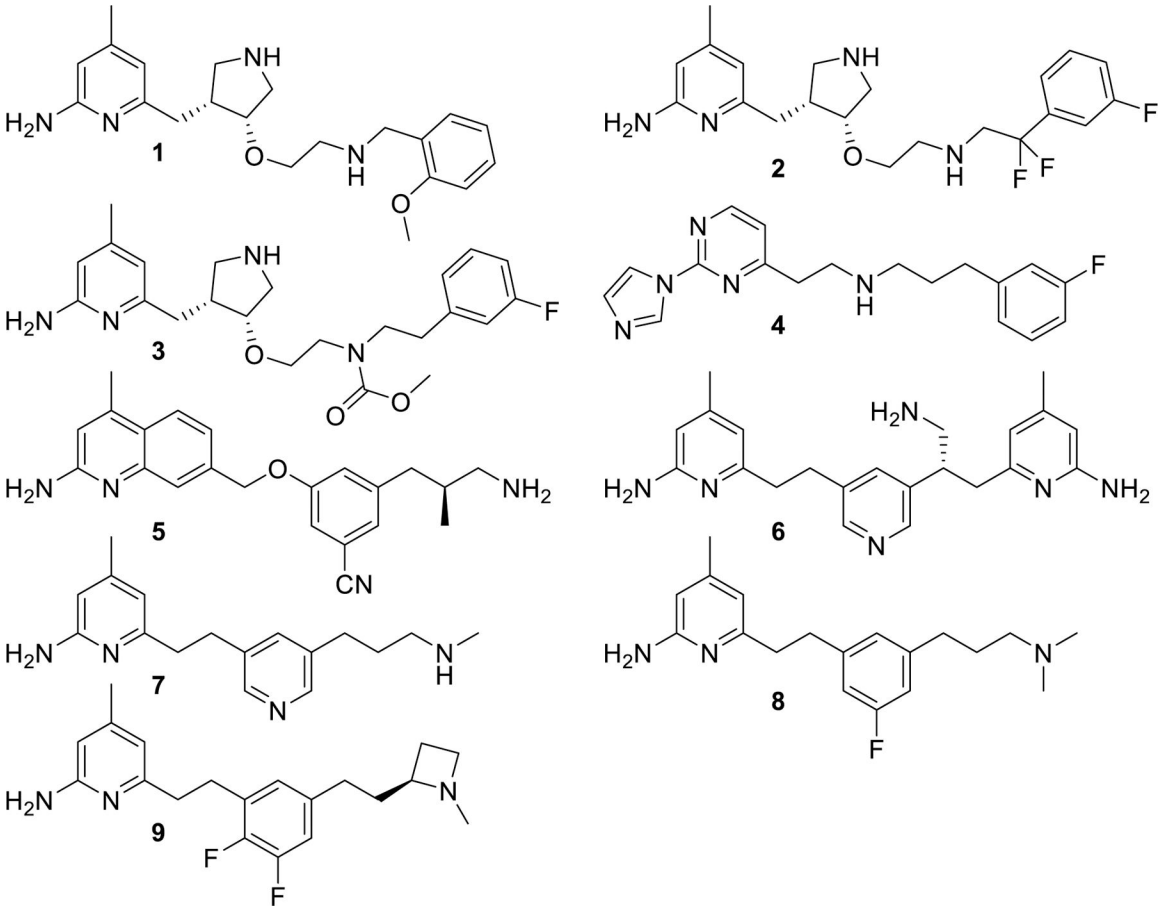

Figure 1.
Structure of recent nNOS inhibitors.

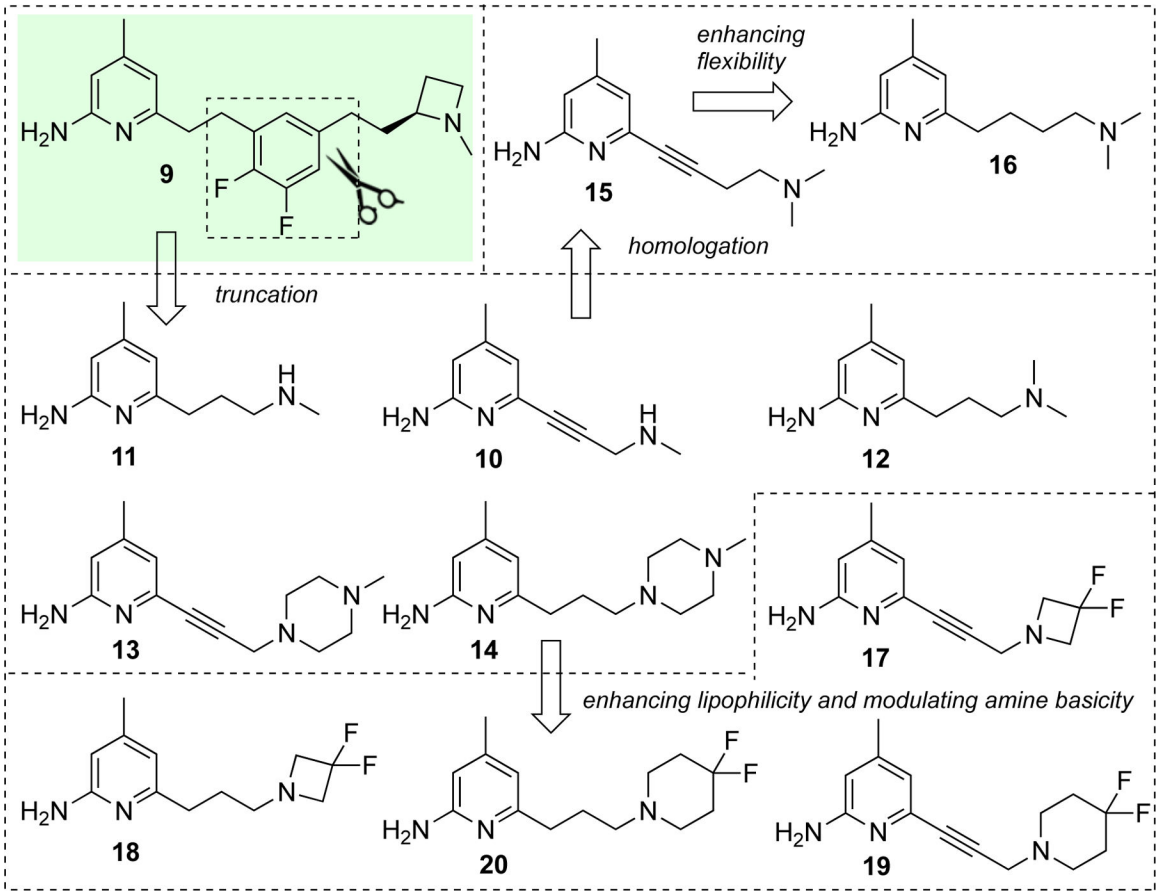

Figure 2.

Analogues from lead **9** with a reduced number of rotatable bonds

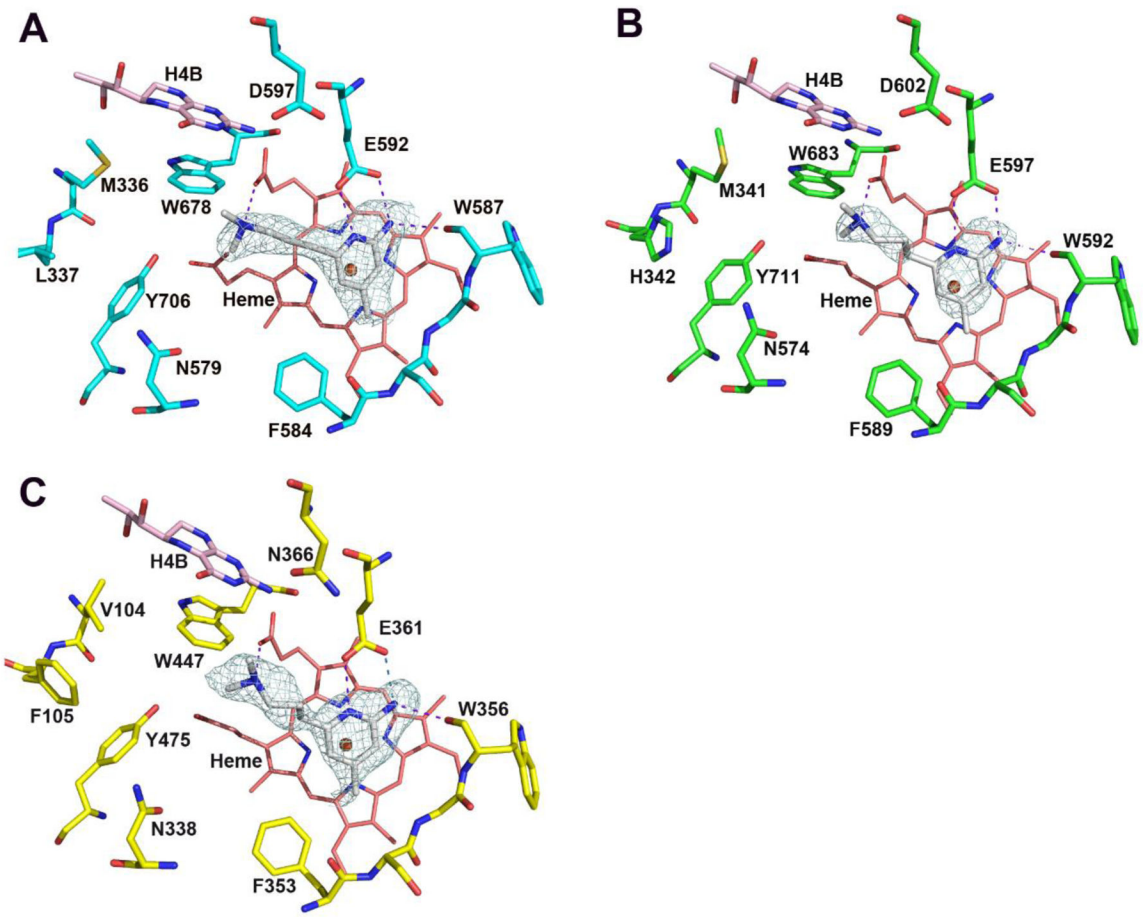

Figure 3.

Active site structures of **12** bound to rnNOS (A), hnNOS (B), and heNOS (C). In all structural figures, the following atomic color schemes are used: cyan, green, and yellow for carbon atoms in the rnNOS, hnNOS, and heNOS backbones, respectively; red, oxygen; blue, nitrogen; light cyan, fluorine. The omit *F*o-*F*c Polder electron density for the inhibitor is shown at the 3.0 σ contour level. Key H-bonds to the inhibitor are depicted with dashed lines.

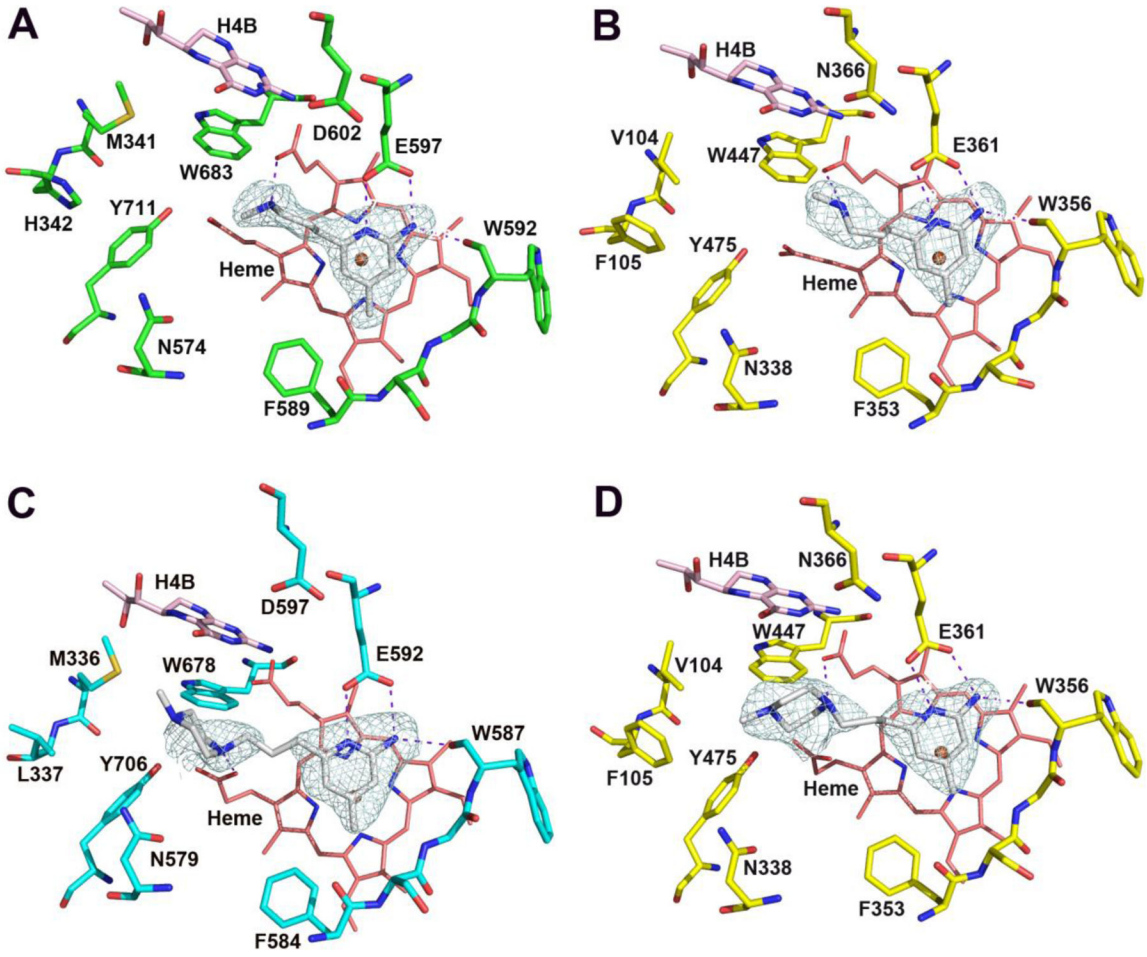

Figure 4.

Active site structures of **11** bound to hnNOS (A) and heNOS (B); and **14** bound to rnNOS (C) and heNOS (D).

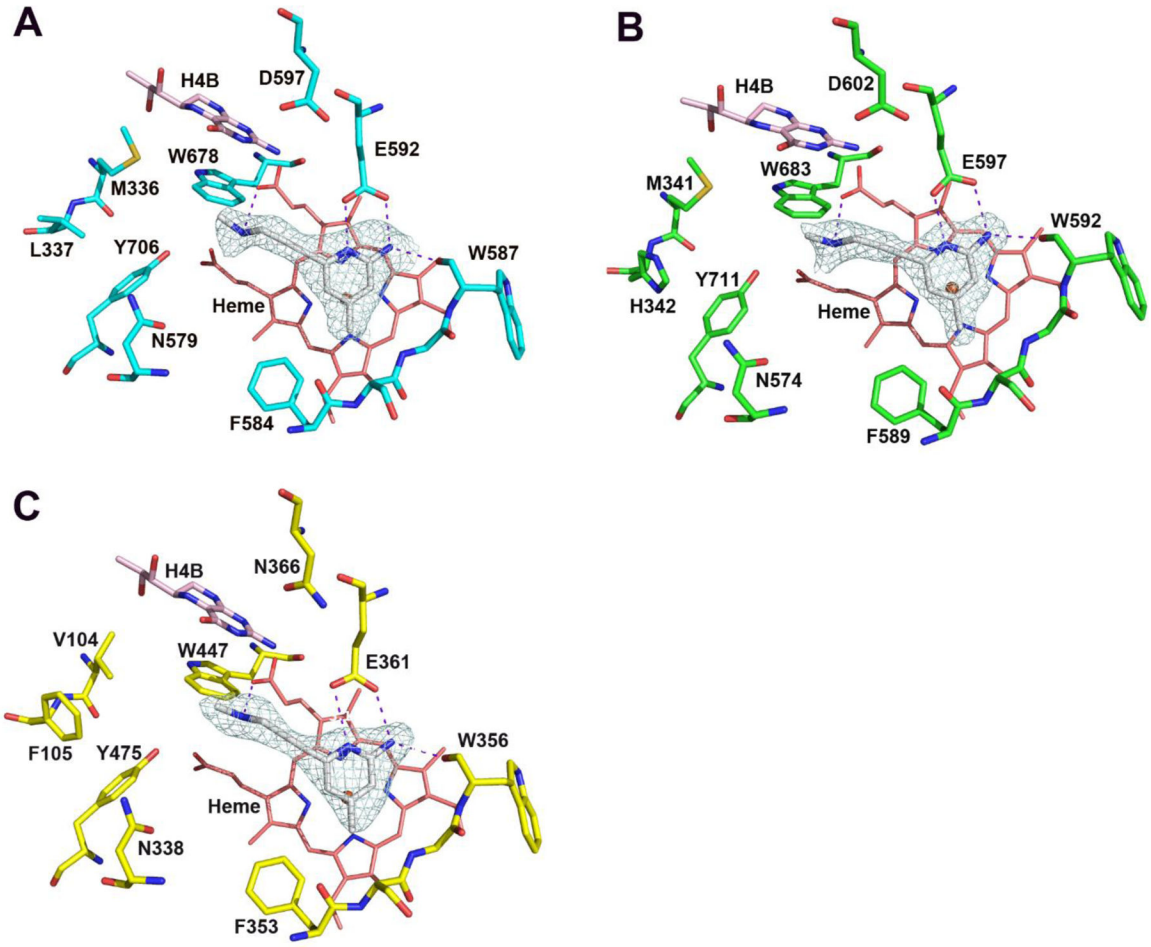

Figure 5.
Active site structures of **10** bound to rnNOS (A), hnNOS (B), and heNOS (C).

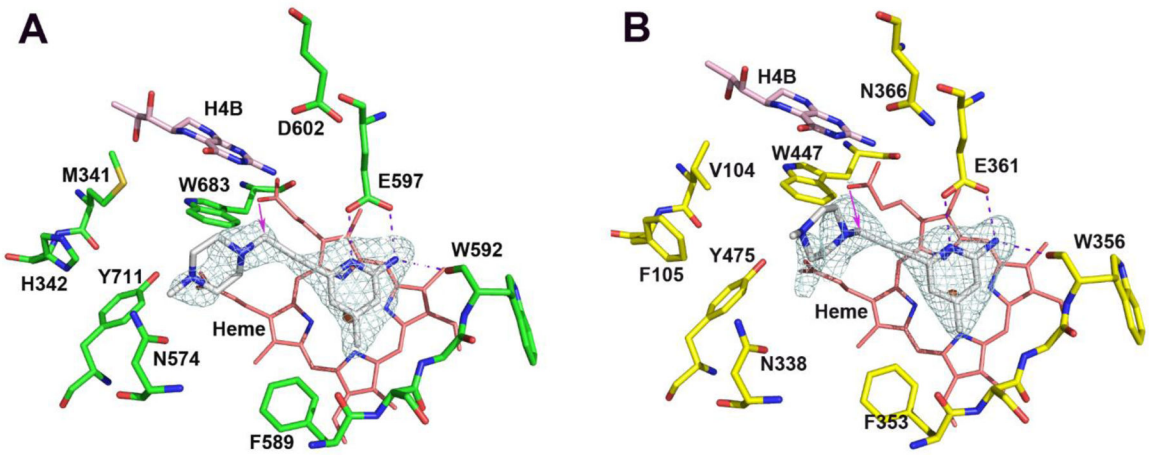

Figure 6.

Active site structures of **13** bound to hnNOS (A) and heNOS (B). The clashes observed between the rigid alkyne linker and propionate A are shown by the pink arrows.

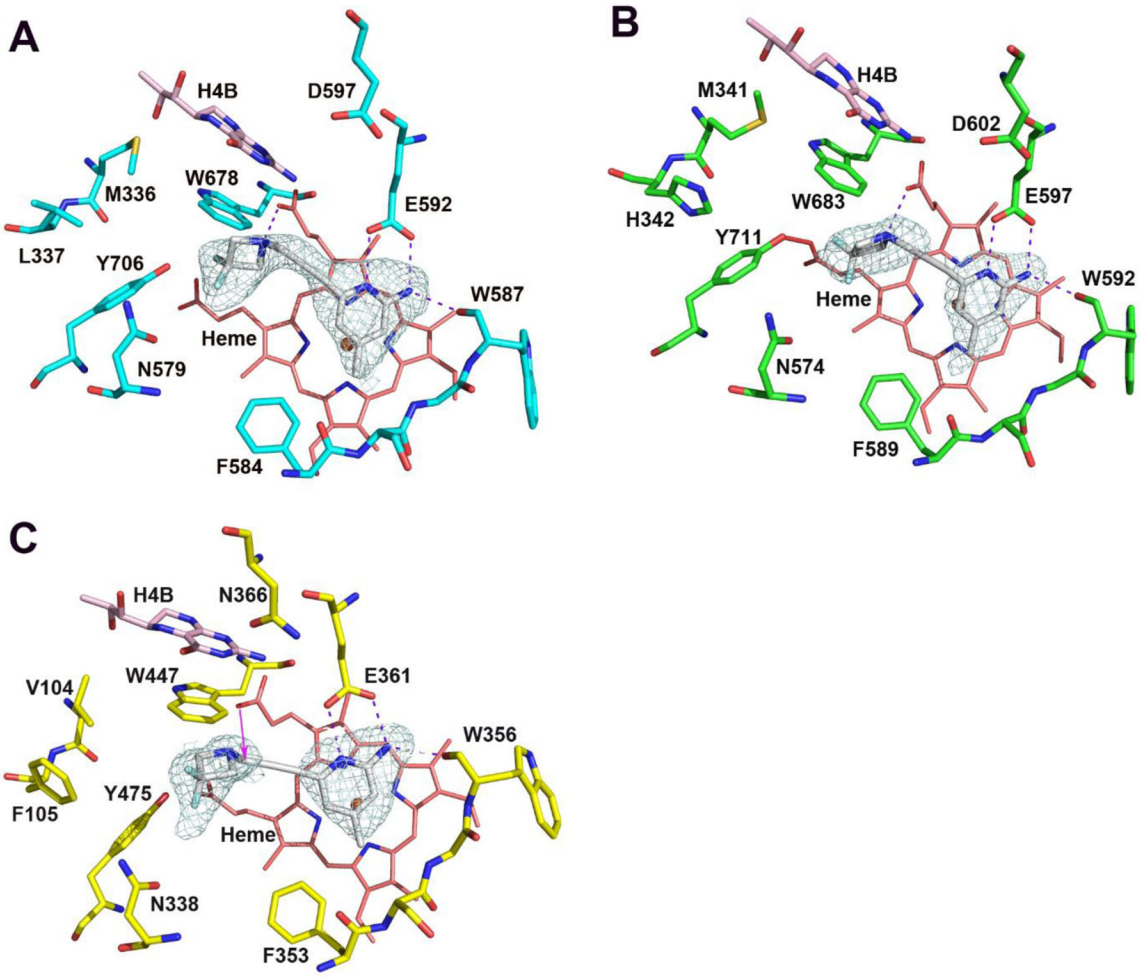

Figure 7.

Active site structures of **17** bound to rnNOS (A), hnNOS (B), and heNOS (C). A clash (pink arrow) was observed between the alkyne linker and propionate A in heNOS.

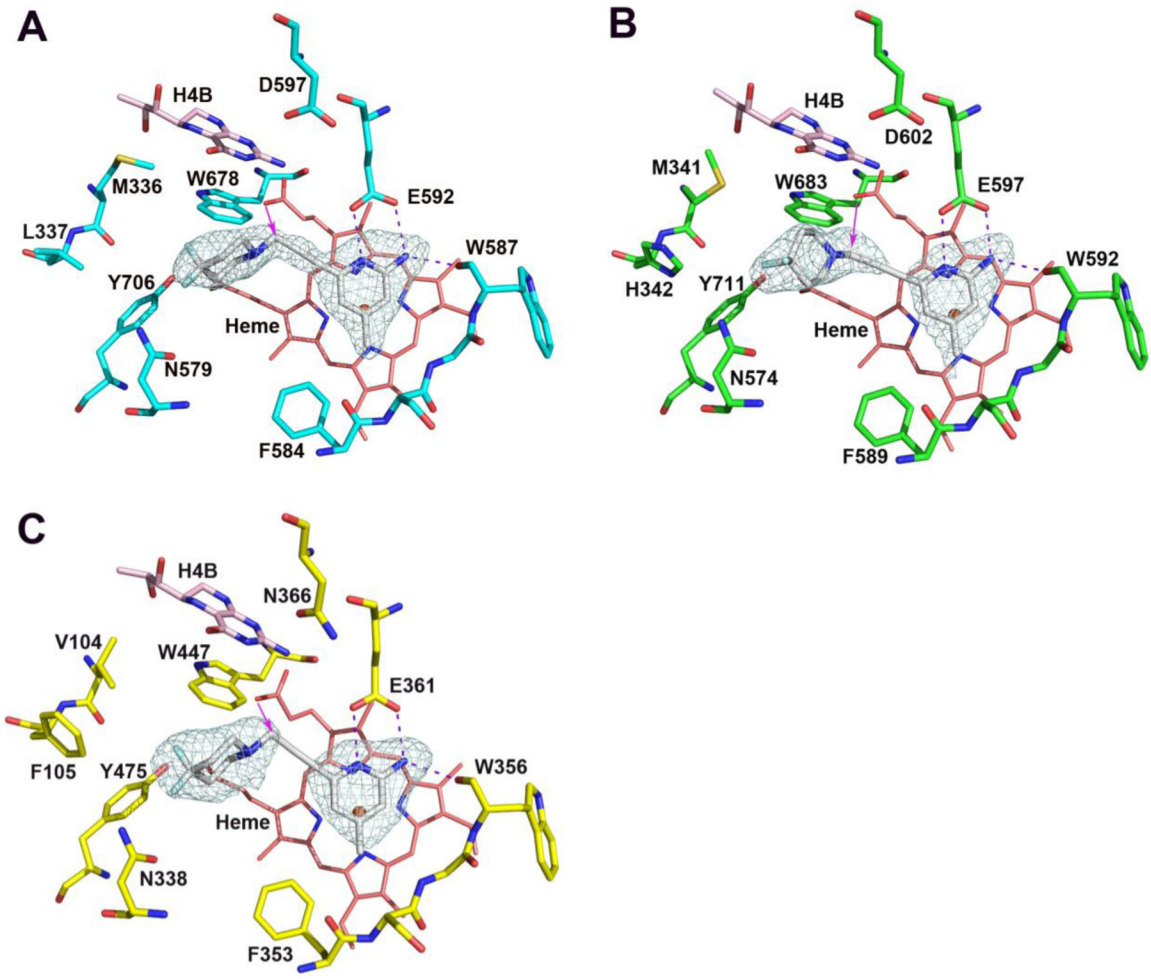

Figure 8.

Active site structures of **19** bound to rnNOS (A), hnNOS (B), and heNOS (C). In all three cases, the clashes of the alkyne linker with propionate A were present (pink arrows).

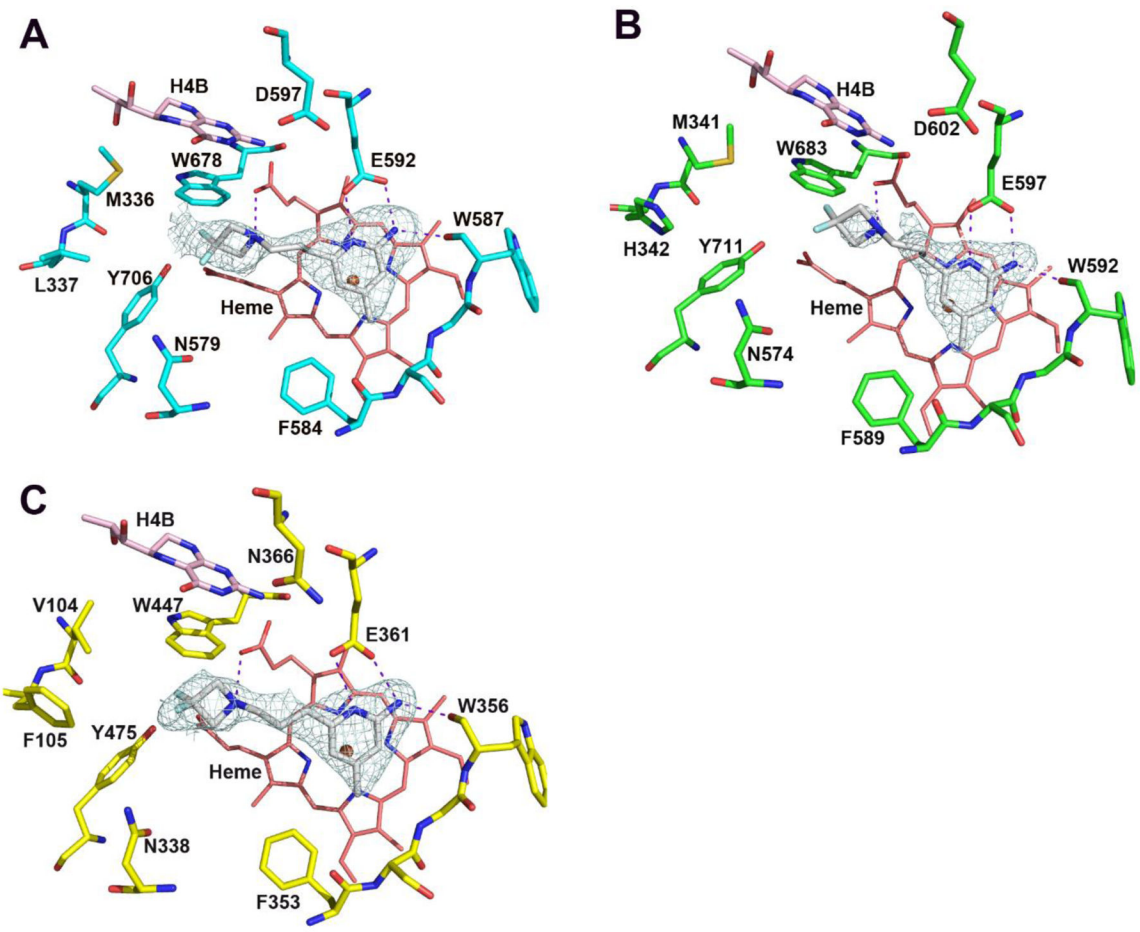

Figure 9.
Active site structures of **18** bound to rnNOS (A), hnNOS (B), and heNOS (C).

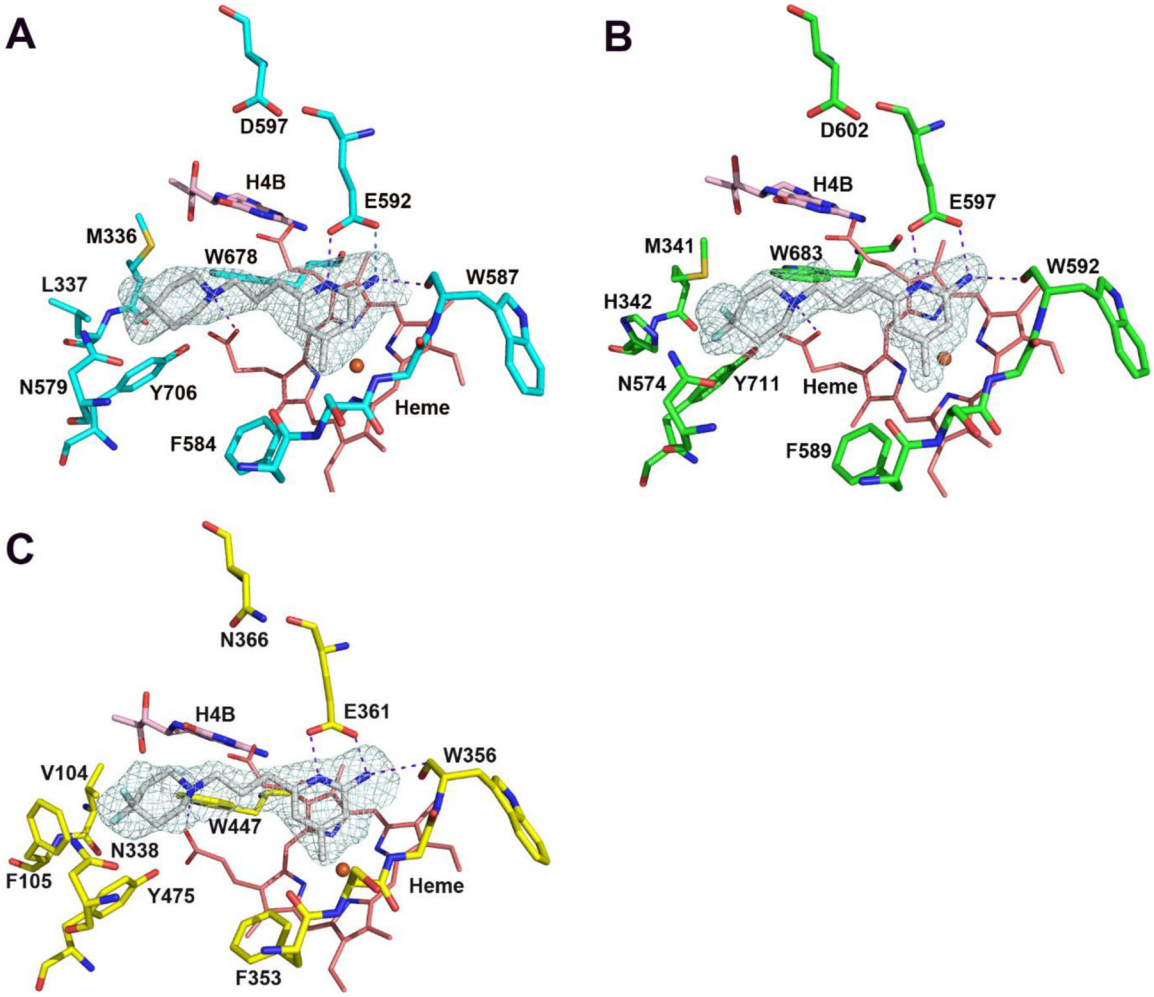

Figure 10.
Active site structures of **20** bound to rnNOS (A), hnNOS (B), and heNOS (C).

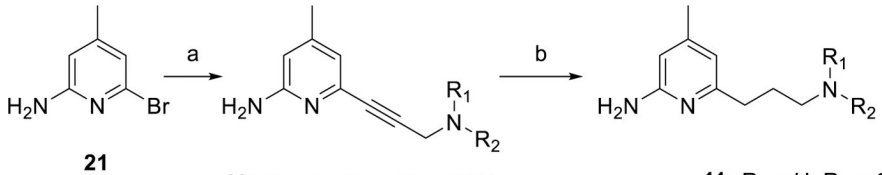

10; R_1 = H, R_2 = CH_3, 61%
13; R_1 = R_2 = -$(CH_2CH_2)_2$-NCH_3, 92%
17; R_1 = R_2 = -$(CH_2$-CF_2-$CH_2)$-, 28%
19; R_1 = R_2 = -$(CH_2CH_2$-CF_2-$CH_2CH_2)$-, 42%

11; R_1 = H, R_2 = CH_3, 89%
12; R_1 = R_2 = CH_3, 84%
14; R_1 = R_2 = -$(CH_2CH_2)_2$-NCH_3, 80%
18; R_1 = R_2 = -$(CH_2$-CF_2-$CH_2)$-, 62%
20; R_1 = R_2 = -$(CH_2CH_2$-CF_2-$CH_2CH_2)$-, 27%

Scheme 1.

General synthetic approaches to compounds **10**-**14** and **17**-**20.** (a) The appropriate propargyl amine, $Pd(PPh_3)_4$ (5 mol%), PPh_3 (10 mol%), CuI (10 mol%), Et_3N, 120 °C, CH_3CN (0.23 M), 24 h, 28–93%; (b) Pd/C or $Pd(OH)_2$/C (10–40 mol%), H_2, CH_3OH, 25–80 °C, 8–24 h, 27–89%.

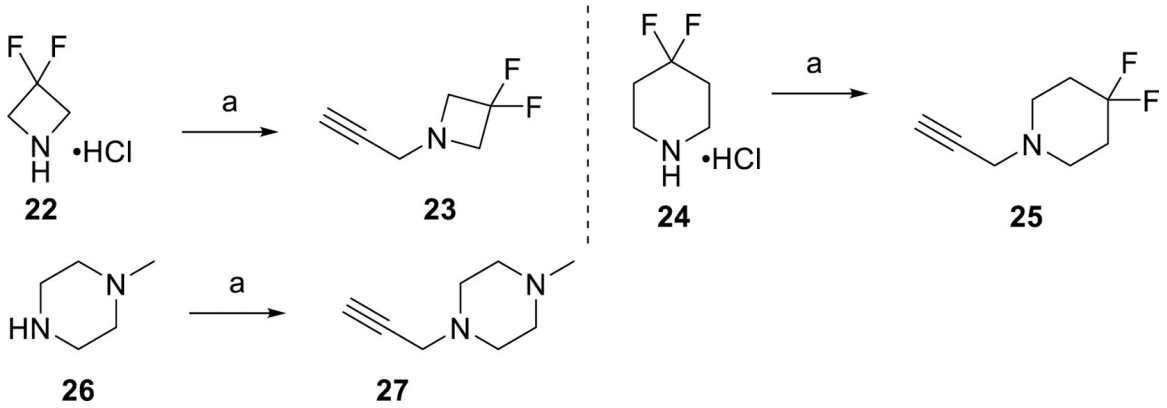

Scheme 2.

Synthesis of propargyl amines **23**, **25** and **27.** (a) propargyl bromide, K_2CO_3, CH_3CN, 25 °C, 8 h, 48–53%.

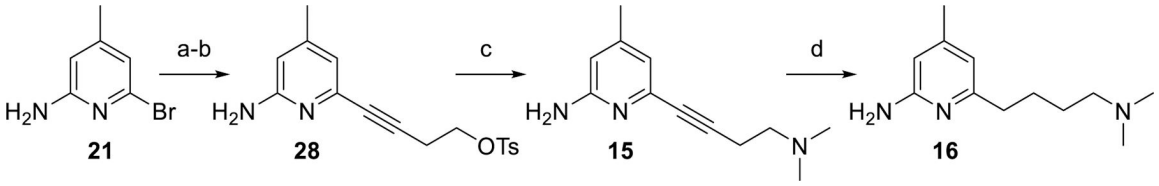

Scheme 3.

Synthesis of compounds **15-16.** (a) But-3-yn-1-ol, $Pd(PPh_3)_4$ (5 mol%), CuI (10 mol%), Et_3N, 120 °C, CH_3CN (0.25 M), 18 h, 70%; (b) TsCl, DMAP, Et_3N, DCM, 0 °C to 25 °C, 17 h, 53%; (c) $(CH_3)_2NH$, K_2CO_3, CH_3CN, 80 °C, 9 h, 68%; (d) Pd/C (10%), H_2, CH_3OH, 25 °C, 24 h, 62%.

Table 1.

List of K_i values and selectivities of **10–20**

Compd	K_i (nM)[a,b,c]				Selectivity		
	rat nNOS	human nNOS	human iNOS	human eNOS	hn/rn	hn/hi	hn/he
10	88	92	3575	1919	1.0	39	21
11	29	21	669	1469	0.7	32	70
12	26	29	2831	3662	1.1	98	126
13	947	2124	113733	43798	2.2	54	21
14	56	171	10160	12536	3.1	59	73
15	242	327	29835	70509	1.4	91	216
16	36	58	7671	7351	1.6	132	127
17	465	488	11089	5132	1.1	23	11
18	95	149	4358	6268	1.6	29	42
19	1591	1430	27369	18950	0.9	19	13
20	**46**	**48**	**6480**	**18639**	**1.0**	**135**	**388**

[a] K_i values were calculated from the IC_{50} values of the corresponding dose−response curves using the Cheng−Prusoff equation. 8 to 11 concentrations were tested, and the IC_{50} value was calculated from an average of at least two duplicates. The standard errors were less than 10%. The ratio hn/rn was determined to evaluate the potential translation of these inhibitors from preclinical data to a clinical study. This ratio was aimed to be as close to 1.0 as possible so that there would be little to no significant difference in the amount of inhibitors used in rat and human dosage. Selectivity values are determined by calculating the ratios of respective K_i values.

[b] The plate reader syringe lines are equilibrated with assay buffer (100mM HEPES, 10% glycerol, pH 7.4–7.5) before the assay.

[c] The assay was performed using assay buffer (100 mM HEPES, 10% glycerol, pH 7.4–7.5), and stock buffer (100 mM HEPES, pH 7.4–7.5).

Table 2.

Effective permeability (P_e) of five commercial drugs and nNOS inhibitors in the PAMPA−BBB assay

Compounds	Reported P_e (10^{-6} cm s^{-1})[a]	Determined P_e (10^{-6} cm s^{-1})[b–d]	Prediction[a]
(±)-Verapamil	16	21.2 ± 0.43	CNS (+)
Desipramine	12	22.8 ± 0.93	CNS (+)
Chlorpromazine	6.5	10.8 ± 0.64	CNS (+)
Dopamine	0.2	0.13 ± 0.14	CNS (−)
Theophylline	0.12	0.1 ± 0.02	CNS (−)
10		4.7 ± 0.44	CNS (+)
11		0.96 ± 0.03	CNS (−)
12		2.0 ± 0.21	CNS (+/−)
13		3.2 ± 0.12	CNS (+/−)
14		2.2 ± 0.01	CNS (+/−)
15		4.1 ± 0.12	CNS (+)
16		2.3 ± 0.04	CNS (+/−)
17		19.6 ± 0.86	CNS (+)
18		17.5 ± 0.71	CNS (+)
19		21.1 ± 0.15	CNS (+)
20		17.3 ± 0.44	CNS (+)

[a]The reported effective permeability (P_e) values from the literature.[53]

[b]All assays were performed over 17 h at a concentration of 200 μM.

[c]All compounds were tested in a triplicate.

[d]Effective permeability values obtained in our in-house conditions.

CNS (+) = high BBB permeation. CNS (−) = low BBB permeation. CNS (+/−) = BBB permeation uncertain.